Journal of Marine Research, 71, 47–82, 2013

Significant internal waves and internal tides measured northeast of Taiwan

by Timothy F. Duda[1,2], Arthur E. Newhall[1], Glen Gawarkiewicz[1], Michael J. Caruso[3], Hans C. Graber[3], Yiing Jang Yang[4] and Sen Jan[5]

ABSTRACT

Internal gravity waves in an area northeast of Taiwan are characterized using data from multiple sensor types. The data set includes intermittent information collected from a ship and short time series from moorings. Modeled nonlinear waves are fitted to observed nonlinear waves to provide self-consistent estimates of multiple wave parameters. A nonlinear internal wave of over 50 m amplitude, observed in deep water, is examined in detail. This wave was moving northward from the southern Okinawa Trough toward the continental shelf, and presumably formed from internal tides propagating northward from the Ilan Ridge area. A possible scenario for the formation of this wave from the internal tide is compared to related behavior south of Taiwan. On the outer continental shelf, a few large internal waves with maximum displacement greater than one-quarter of the water depth were measured with moorings. Sensors aboard ship and satellite recorded waves in this area traveling in many directions. Two possible causes (not mutually exclusive) for the multiple wave directions are scattering of nonlinear internal waves arriving from the south, and variable local generation of nonlinear gravity waves by the strong tidal and internal tidal currents. Internal tides on the shelf are relatively strong, among the strongest measured, having about 10 times greater kinetic energy density than numerous low-energy sites, which is consistent with the strong barotropic tides of the area. The ratio of diurnal baroclinic to barotropic kinetic energy found in this area is unusually high.

1. Introduction

Internal waves northeast of Taiwan are known to be strong, yet detailed in situ data describing these waves are sparse. Both northeast and south of Taiwan, abrupt changes from deep to shallow water, coupled with energetic tides, cause some of the highest amplitude internal waves known, with many large waves observed south of Taiwan in the Luzon Strait

1. Woods Hole Oceanographic Institution, Woods Hole, Massachusetts, 02543, USA.
2. Corresponding author ***e-mail: tduda@whoi.edu***
3. Rosenstiel School of Marine and Atmospheric Sciences, University of Miami, 4600 Rickenbacker Causeway, Miami, Florida, 33149, USA.
4. R.O.C. Naval Academy, Tsoying District, Kaohsiung, 813, Taiwan, (R.O.C.).
5. Institute of Oceanography, National Taiwan University, No. 1, Sec. 4, Roosevelt Rd., Taipei, 10617, Taiwan (R.O.C.).

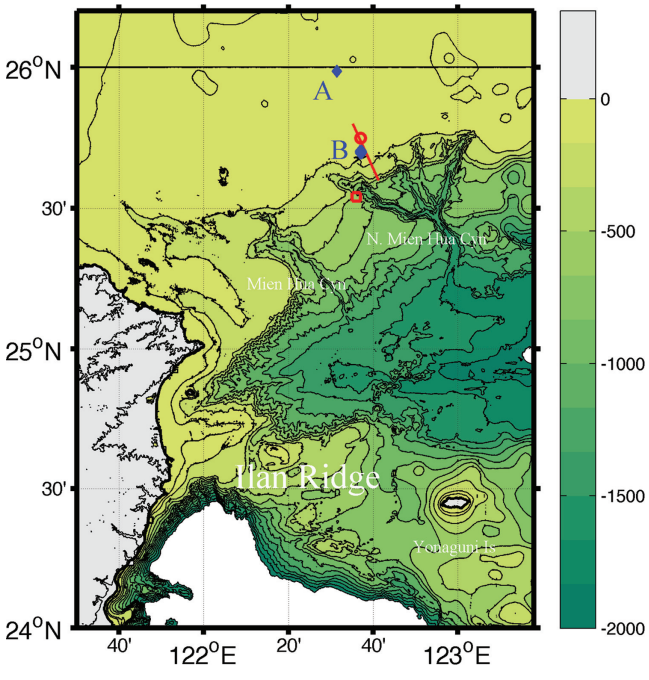

Figure 1. A chart of the study area is shown. Sites A and B (mooring areas) are marked with blue diamonds. A larger area is shown in Figure 3. Site B is a short distance north of the west branch of North Mien Hua Canyon. The red square shows the site of an encounter with a nonlinear wave south of the shelf, analyzed in Section 4. The circle shows the site of an encounter with a shelf internal wave as the ship was moving south. (The track line is shown.) The depth contour interval is uniform at three per 500 m, with an additional 100 m contour added with no color change. (For orientation, the depth at Site B is 130 m.) The white area at the south is deeper than 2,000 m. Yonaguni Island is the westernmost of the Yaeyama Islands, most of which lie east of the charted area. The line at 26° N is an artifact of a database change.

and in the South China Sea (Li and Farmer, 2011; Ramp et al., 2010; Duda et al., 2004; Klymak et al., 2006). The areas northeast and south of Taiwan have basic similarity, but the details of the forcing currents and the bathymetry differ between the two regions (Niwa and Hibiya, 2004), and the resulting internal waves northeast of Taiwan are less energetic than the South China Sea counterparts, although still large. Comparing and contrasting internal waves in the two areas is helpful for exploring the dependency of internal wave generation and evolution on the many pertinent parameters. Multiple internal waves observed east-northeast of Taiwan are examined here, providing information regarding wave properties, including energy, amplitude and direction of propagation.

The study region includes a continental shelf north of a (curved) line, extending from the northern edge of Taiwan, which is directed slightly north of east (Fig. 1). Canyons incise the curved shelf edge. To the south of the shelf is the southern Okinawa Trough, and to the

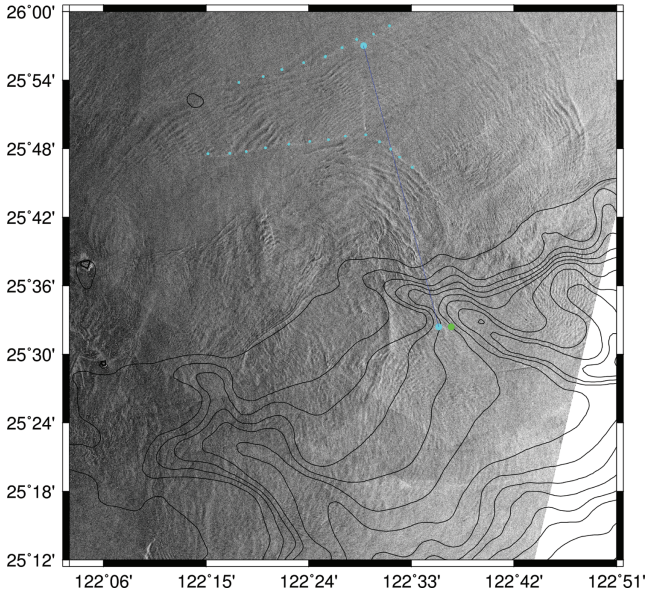

Figure 2. An ERS2 satellite SAR image is shown for the date and time Sept. 7, 2009 02:27 UTC. 100 m depth contours are shown. The canyon to the west is Mien Hua Canyon. The branched canyon to the east is North Mien Hua Canyon. This reproduction has 150 m resolution, which has been chosen to clarify the internal wave features. The lines of dots show wave packet boundaries discussed in the text.

south of the trough is the Ilan Ridge, which extends eastward from Taiwan and connects to another ridge heading to the east/northeast. A field effort was undertaken in this area in 2009 as part of a program called Quantifying, Predicting and Exploiting Uncertainty (QPE, Gawarkiewicz et al., 2011), and data from this effort are analyzed here. This area was chosen for the program in part because of a prominent intermittent relatively cold feature in the area northeast of Taiwan called the cold dome (Jan et al., 2011), and also because of the variable nature of the Kuroshio currents that impinge on the continental slope. In the field effort, in-situ sensor moorings were in place for two five-day periods (roughly) in the span of Aug. 24 to Sept. 10, 2009, and acoustic Doppler current profilers were in place for a longer time, measuring conditions (including internal waves) in support of underwater sound propagation studies. Additional internal wave measurements were made with instruments aboard a ship and with satellite sensors.

Figure 2 shows a synthetic aperture radar (SAR) image of the area made with data from the ERS2 satellite. Dark/light banding in SAR images can often be attributed to varying surface roughness in the alternating zones of divergent and convergent surface currents of mode-one nonlinear internal waves (Porter et al., 2001). The upper middle portion of Figure 2 shows waves of elevation that appear to be heading in a north-northwest direction

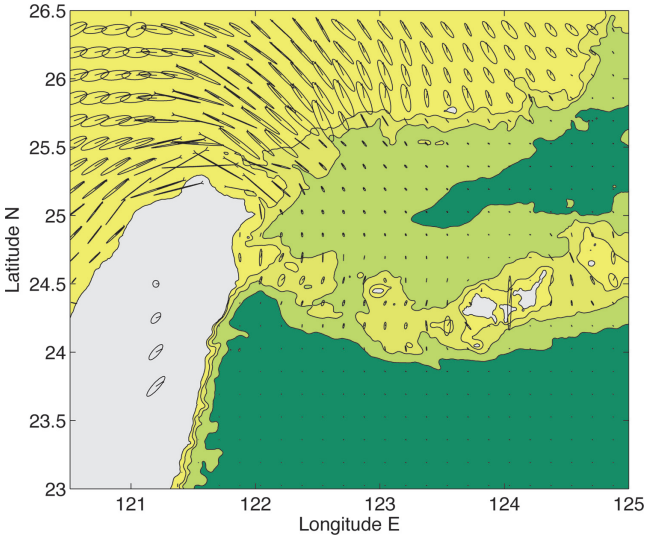

Figure 3. M_2-constituent semidiurnal barotropic tide ellipses are plotted. Depth is contoured at 200, 700 and 2,000 m, with the dark shade marking areas deeper than 2,000 m. The scale is shown by four ellipses plotted over Taiwan, with semi-major axes of 10, 20, 30 and 40 cm s^{-1}. Each scale ellipse has semi-minor axis 10 cm s^{-1}, inclination 45° and phase 45.

(dark first), consistent with QPE observations there of the thermocline being below the center of the water column. Between Mien Hua Canyon at 122° 20′ E and the west branch of North Mien Hua Canyon at 122°40′ E there is a wave group that appears to be moving to the south, and two packets can be seen to be moving to the northeast, one after the other, from the west branch. This remarkable image shows that there are many sources and fates of internal waves in this area. A few features of internal waves measured in the area with the modest set of observations are described in the sections to follow.

Tidally forced time-varying density anomalies reach significant strength where predominant currents flow across bathymetric ridges in the Taiwan area, the anomalies being a direct consequence of significant vertical water excursion. This is the root cause of the large tidally driven internal waves that have been observed in detail south of Taiwan. The QPE area examined here has some similarities to the better measured area south of Taiwan. Figure 3 shows principal lunar semidiurnal period (M_2, 12.42 hr) barotropic tidal ellipses for the QPE, extracted from the Oregon State University "Yellow Sea" regional tidal inverse (www-po.coas.oregonstate.edu/research/po/research/tide/, last viewed Jan. 28, 2013; Egbert and Erofeeva, 2002). The large currents directed normal to the ridge crest at the Ilan Ridge and the Yaeyama Islands drive energetic internal tides, as do the large currents at the slope near the QPE site. These internal tides have been modeled numerically (Niwa and Hibiya, 2004 [M_2 period only]; Lermusiaux et al., 2010), but many of their detailed properties have been unknown.

As a result of the strong barotropic tidal currents and the topography, the internal tides on the shelf area have kinetic energy values (per unit area of seafloor) that are significantly greater than at a relatively benign shelf site in the Mid-Atlantic Bight, east of the United States, studied in 2006, but are somewhat less than recorded in the South China Sea (Duda and Rainville, 2008). Nonlinear internal waves at the site are of intermediate energy, being larger than those observed at, for example, the Mid-Atlantic Bight (Apel et al., 1997; Shroyer et al., 2011; Shroyer et al., 2011) and the Celtic Sea shelf break (Green et al., 2008), but smaller than those of the northern South China Sea. Thus, the site has some unique internal wave effects, at least in comparison with those other sites, with some of the effects explored here in detail. Waves both approaching the shelf and on the shelf are examined here, while internal tides south of the shelf in deeper water are the subject of a companion paper (Lien, Sanford and Jan, 2013).

The measurement systems are described in Section 2. Section 3 is an overview of tidal current and internal wave response. Detailed findings appear in the subsequent sections. Findings reported here are: 1) Characteristics and probable cause of one intermediate-sized nonlinear wave observed in deep water moving northward toward the shelf (Section 4); 2) Direction and amplitude characteristics of internal waves on the shelf (Section 5), with the best-measured individual nonlinear wave characterized in detail; and 3) Energies of internal tides on the shelf (Section 6).

2. Observations

Complete information on the measurements is available in a technical report (Newhall et al., 2010). Information about the subset of data utilized here is given in this section. All work was performed using the ship *RV Ocean Researcher 1* (*OR1*) from National Taiwan University, Taipei. There were two cruise legs for the QPE on-shelf exercise (Aug. 23, 2009 to Sept. 1, 2009 and Sept. 4, 2009 to Sept. 12, 2009), with a port stop between them. Moorings were placed at two locations, chosen to support the QPE underwater acoustics exercise. The locations were called Site A and Site B. (Fig. 1). Location and sampling duration information for the moorings is listed in Table 1. The depth at Site A was approximately 112 m, and the depth at Site B was approximately 134 m.

Teledyne-RDI (San Diego, CA) Workhorse acoustic Doppler current profilers (ADCPs) were placed on the seafloor at each site, which were left in place during the port visit. The ADCPs were 32.65 km apart, with a heading from ADCP-A to ADCP-B of 163.8°. A third ADCP was placed by Taiwan Naval Academy southwest of Site B, where the water depth was 149 m. Other moorings were in place only while the ship was in the area because of the high likelihood of them being damaged by fishing activity if left unattended. (Despite the brief deployment, most of the sensors on two moorings were heavily damaged; see Table 1 and the technical report.) The short durations of many of the mooring emplacements makes their data less than ideal for tidal and internal tidal analysis. (One month or longer duration is desirable). The short durations also do not allow full characterization of the variable

Table 1. Moored sensor parameters. T, P, C are temperature, pressure and conductivity sampled once per minute. Symbols indicate that the mooring was dragged to a new location (†) or dragged and damaged (*).

Mooring	Latitude, deg-min N	Longitude, deg-min E	Sensors	Deploy date	Recovery date	Duration, days
Site A ADCP	25-59.323	122-31.525	Velocity, 3 min/sample	29 Aug	9 Sept	11
Site A El leg 1	25-59.059	122-31.574	T,P,C	29 Aug	30 Aug	1.5
Site B ADCP	25-42.334	122-36.961	Velocity, 3 min/sample	24 Aug	10 Sept	16.5
Site B El leg 1	25-42.549	122-36.866	T,P,C	24 Aug	28 Aug	4 *
Site B E2 leg 1	25-42.505	122-37.454	T,P,C	24 Aug	28 Aug	4 *
Site B E3 leg 1	25-42.051	122-37.117	T,P,C	25 Aug	28 Aug	4 †
Site B El leg 2	25-42.541	122-36.842	T,P,C	4 Sept	9 Sept	4.5
Site B E2 leg 2	25-42.519	122-37.444	T,P,C	4 Sept	9 Sept	4.5
Site B E3 leg 2	25-42.049	122-37.104	T,P,C	4 Sept	9 Sept	4.5
SW Site B ADCP	25-40.101	122-35.002	Velocity, 1 min/sample	14 Aug	9 Sept	27

nonlinear internal wave field. However, the scarcity of data of this type makes the mooring measurements valuable. (The high fishing activity is one reason for the scarcity.) Note finally that two ADCP's averaged pings for three minutes, and thus could not temporally resolve currents in short nonlinear internal waves passing overhead.

The vessel *OR1* was equipped with a system to record images of the ship's navigation radar once every five minutes. The images had a diameter of six nautical miles, and resolution of 14.6 meters per pixel. Radar echoes (scatter) from rough surface waves associated with surface current convergences within internal waves were seen in many images. Backscattering from internal-wave roughness variations is distinguishable from backscattering of other origin by its signature moving linear pattern.

The vessel *OR1* was also equipped with a Simrad (Horten, Norway) EK500 fishery research echo sounder (sonar). Echo returns from this instrument were recorded as images displaying echo strength as a function of depth z and time t. Here, images with maximum echo ranges (z limit) of 180 m and 500 m are analyzed, with images typically covering 22 minutes. Scattering from zooplankton will dominate these images (Lavery et al., 2007), so that to the degree that layers of passive zooplankton (i.e. not swimming) are identifiable, rapid vertical migration of the layers will indicate vertical transport of water within internal waves.

A few dozen satellite remote sensing images were collected during the experiment period. Here, one synthetic aperture radar (SAR) image is utilized (Fig. 2). This has spatial resolution of approximately 30 m. Additionally, one Moderate Resolution Imaging Spectroradiometer (MODIS) satellite image with approximately 500 m resolution is used. Under proper conditions MODIS images show good sunglint visualization of internal waves (Jackson, 2007).

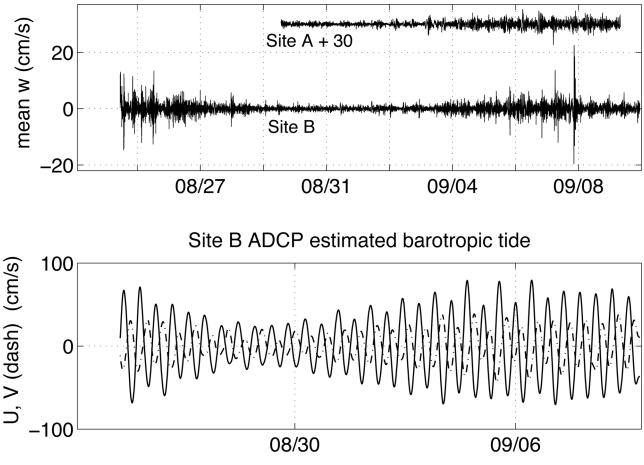

Figure 4. Time series of all-depth means of ADCP vertical velocities are shown at the top. Estimated Site B barotropic tidal current is shown at the bottom, U (eastward) and V (northward, dash).

3. Overview of tidal forcing and response

Before showing the detailed internal tide and nonlinear internal wave responses, the forcing barotropic tidal currents in the area are shown (Fig. 4). The lower panel of the figure shows the depth average of tidal frequency band currents measured with the Site B ADCP; data from this instrument are from the depths of 36 to 120 m only, representing 64% of the water depth, so that the plotted values are only estimates of the barotropic tidal currents. The peak current speeds of about 84 cm s^{-1} at Site B are greater than those at a roughly comparable South China Sea site [the Asian Seas International Experiment-South China Sea ASIAEX-SCS area, (Beardsley et al., 2004)] by a factor of three or four. The primary Site B sampling interval includes two periods of strong currents (spring tides), but only the latter portion of the first spring tide was measured. The second spring tide featured the strongest currents, peaking from Sept. 4 to 6.

The difference in tidal current strength between QPE Site B and ASIAEX-SCS can be explained by the bathymetry. The cotidal charts in Beardsley et al. (2004) show that semidiurnal and diurnal surface tidal waves arrive from the east and pass to the north and south of Taiwan. There is significant dissipation over the two ridges in the Luzon Strait south of Taiwan. West of the strait the wave enters the rather large South China Sea, so the energy (per unit length) incident on many shelf edges around this sea is small, and the currents are moderate. A notable exception is the M_2 constituent that moves into Taiwan Strait as a Kelvin wave and creates significant currents. On the contrary, the currents of the surface tidal waves passing north of Taiwan are only moderately affected by passing over the Ilan/Ryukyu ridge feature and are quite strong as they move into shallow water and impinge on the Chinese coast and refract counterclockwise into the Taiwan Strait.

The strong tidal currents in the QPE region generate internal tides (Niwa and Hibiya, 2004), which can then spawn nonlinear internal waves (e.g. Holloway et al., 1999). These nonlinear waves are ubiquitous in the QPE area. These waves can be uniquely identified in ADCP records by studying the depth-averaged vertical velocities $w(z)$. This is because the waves tend to be mode-one internal waves riding on the thermocline of high buoyancy frequency $N(z)$, so that vertical averaging coherently sums the signal while mitigating the non-negligible measurement noise. In Figure 4, the time series of depth-mean Site A and Site B w show activity well correlated with the tidal forcing. Individual packets or pulses of high activity can also be identified in the data. Although the data are good indicators of nonlinear internal wave activity, some of the high-frequency variations in velocity are attenuated by the three-minute ADCP averaging. Therefore, these data cannot be used for detailed nonlinear internal wave studies. The one-minute data from the other ADCP are slightly noisier and do not improve the packet imaging.

The stratification ($N(z)$) has an important impact on internal wave characteristics because it defines the potential energy conditions that the waves disturb, and thus the restoring forces. Figure 5 shows temperature, salinity, density and density gradient profile data from two stations. These data indicate a strong pycnocline situated near the surface in both deep and shallow areas. This is a dynamic and rapidly changing area (Gawarkiewicz et al., 2011), and these conditions varied on time scales as short as a day during QPE. The $N^2(z)$ profile data shown here will be used to compute nonlinear wave shapes later. Note that there is an upper layer of reduced salinity at both stations, possibly unusual for the area and likely to be related to Typhoon Morakot (Gawarkiewicz et al., 2011). To judge the unique salinity effect, profiles of $N^2(z)$ computed with the salinity portion of the density gradient removed are also shown. Removing the salinity contribution would reduce the maximum density gradients by 22% and 36% for the canyon and shelf stations, respectively.

4. A nonlinear solitary wave in deep water

a. Wave measurements

A few dozen nonlinear wave packets or individual nonlinear waves are recognizable in the collection of the ship's radar images. Two wave events were encountered in water deeper than 300 m. The largest and best measured of the two was a single (solitary) wave encountered over the West Branch of North Mien Hua Canyon during a night acoustics exercise. The location is shown by a red square in Figure 1. Figure 6 shows a color-altered version of one of the series of radar images of the wave, superimposed on a distance scale. Tracking wave motion in the series of georeferenced images shows the wave to move northward at 2.0 m s^{-1}, propagating towards bearing 347° (the direction normal to the crest).

Figure 7 shows two contemporaneous images made with the echo sounder data. (These were made with the same ping data; the scales differ.) The wave is evident in the backscatter return. The lines on the images show wave displacements for a computed theoretical wave shape, to be explained later. The width of the wave and the displacements in the wave can

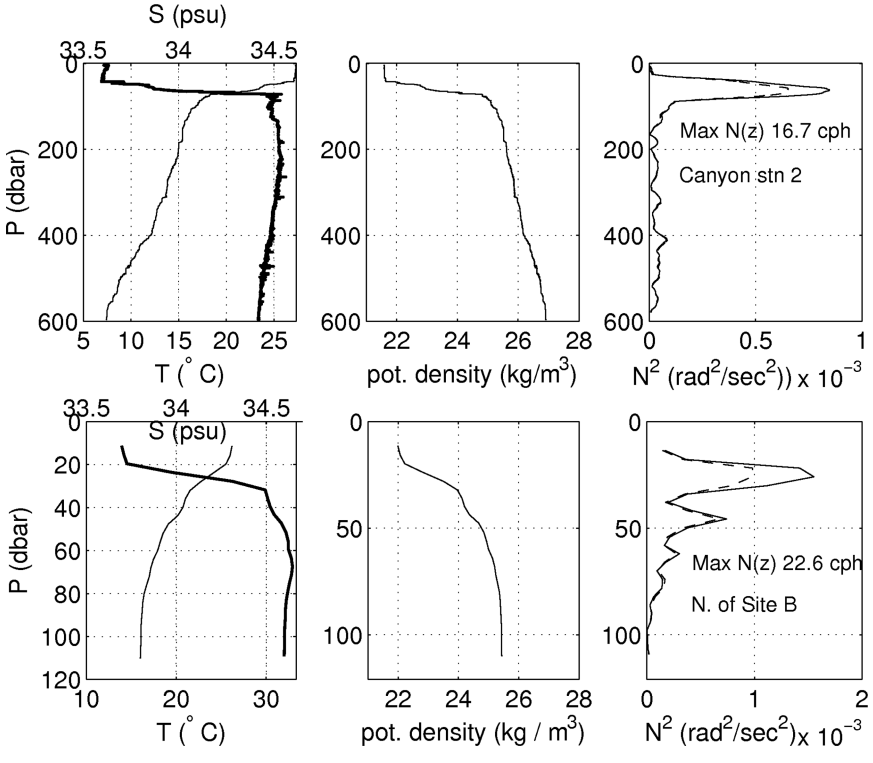

Figure 5. Stratification data from two stations are shown. At the top are lowered CTD data from Station 2 in North Mien Hua Canyon (25° 26.99′ N, 122° 16.07′ E, water depth 615 m, Sept. 10, 2009, 21:08 UTC). At the bottom are processed Seasoar data from north of Site B (25° 45.05′ N, 122° 36.60′ E, Aug. 26, 2009, 04:07 UTC). At the left, the thick lines show salinity, thin show temperature. At the center, the potential density profiles are shown. At the right, the lines show $N^2(z)$, and the dashed lines show fictional $N^2(z)$ computed with the T profiles as shown and $S = 35$.

be estimated from the sonar and radar data. The echoes from the upper layer are seen to migrate downward and then upward approximately 50 m in about a 10-minute period. The resolution limits of the system preclude other quantitative analyses of the wave using only these data. The data are adequate, however, to guide a modeling exercise, with the fitted wave providing useful information (next two sections). The time of maximum depression in the echogram is 19:57 UTC on Sept. 6, 2009. This is 03:57 local time on the 7th. The ship position at this time was 122.608° E, 25.54° N (122° 36.48′ E, 25° 32.4′ N), approximately 17.3 km south of Site B (122.62° E, 25.705° N), at heading 175°. The wave location is 85 km north of the steep northern edge of the Ilan Ridge plateau, and 140 km north of the plateau's southern edge (Fig. 1). Because the water depth at this location is about 580 m, it can be inferred that this is a transbasin wave approaching the shelf, possibly generated in

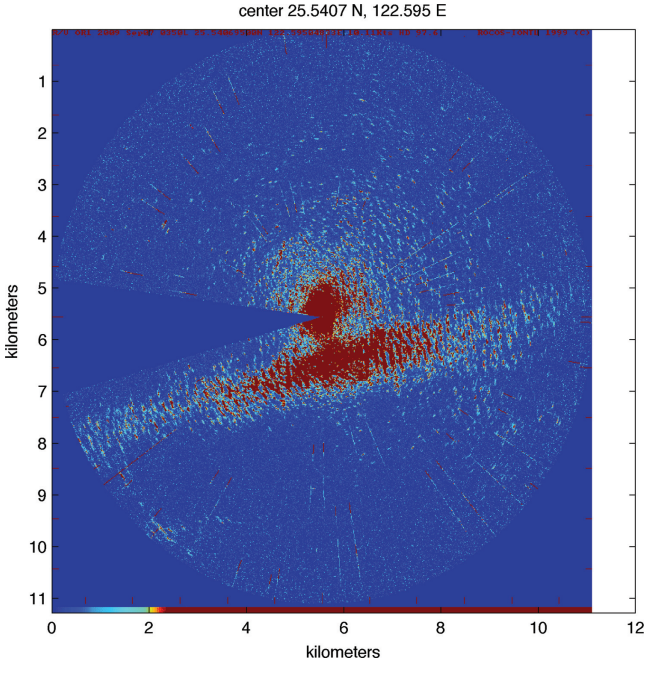

Figure 6. A ship radar snapshot is shown, depicting surface roughness from converging currents in a nonlinear internal wave. This is one of a series. The ship location is at the center. North is upward. The ship heading is east. A stern radar shadow is visible.

deep water from northward-directed internal tides originating at Ilan Ridge. Such internal tides have recently been modeled (Lermusiaux et al., 2010).

Wave shapes can be expressed in terms of streamline displacements in the $[x, z]$ plane. Thus, the time series sonar intensity images $I(t, z)$ need to be converted using $dx/dt = v(t)$, where v(t) is the time-dependent speed of the ship, in the reference frame of the moving wave, projected onto a line parallel to the wave propagation direction. The ship was holding station until just prior to the arrival of the wave, when it started moving at steady speed and direction, traveling 5.1 m s^{-1} at course 102° (re true north) while passing through the wave. Using trigonometry, the ship velocity, and the observed wave velocity of 2.0 m s^{-1} at heading 347°, the speed $v = 2.6$ m s^{-1} is found. The procedure can be understood in terms of wave backpropagation. The point q in space, where the ship exits the wave, is relocated to its position b at the time the ship entered the wave while at position a. The distance $\overline{ab}$ and the transit time are used to find the solution. By chance, the ship velocity and v are constant while this particular wave passes, so the images of the wave in Figure 7 are undistorted and they do not require complicated adjustment to compare with computed wave shapes.

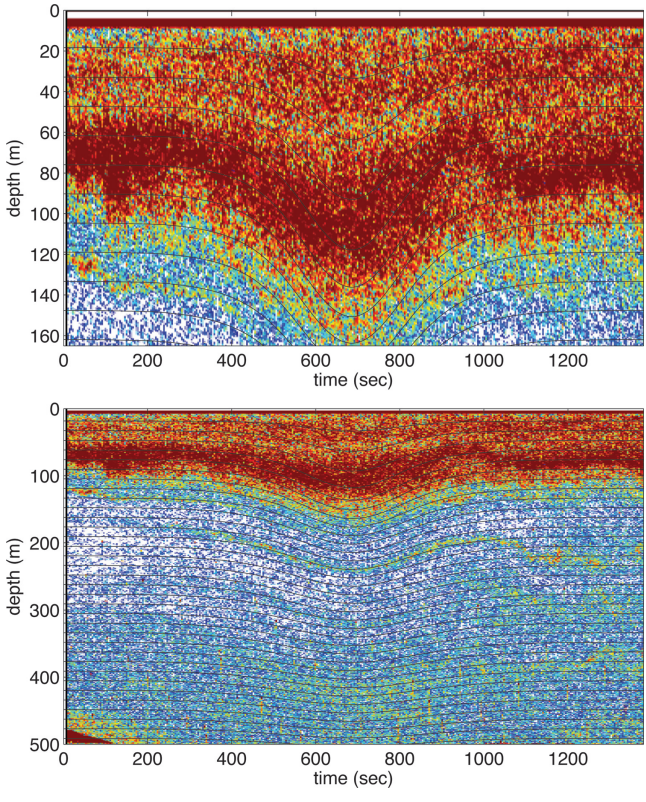

Figure 7. A time series of backscatter records from the EK500 echo sounder is plotted. Red (or dark in grayscale), largely at shallow depths, indicates strong echo. The upper panel shows the upper 165 m of depth. The lower panel shows the same data plus additional later arriving echos. The seafloor return can be seen near time zero of the lower panel. The black lines are streamlines of a permanent form solution of the DJL equation that fits well with the apparent echo displacements. Note specifically the echo line at approximately 200 m depth. The maximum depression of strong echo is at 19:57 UTC on Sept. 6, 2009.

The wave is difficult to identify in the ERS2 SAR image examined earlier (Fig. 2), taken 6.5 hours after the ship-based wave measurement. A line connects the location of the ship/wave encounter with a point 47 km to the north at heading 347°, which would be the wave location if it had continued to move at 2.0 m s^{-1} as determined from the radar image sequence. The northward tidal advection in this time interval would be 6 km, computed from estimated Site B ADCP barotropic tides. An average celerity of 1.75 m/s over the 6.5 hour interval added to this advection would place the wave in the same position. Nonlinear internal waves heading north-northeast are evident at the northern terminus of the line, with a possible leading wave crest highlighted with small dots. These may be evolved from the wave measured at the ship, although we judge this unlikely, as the wave celerity is expected

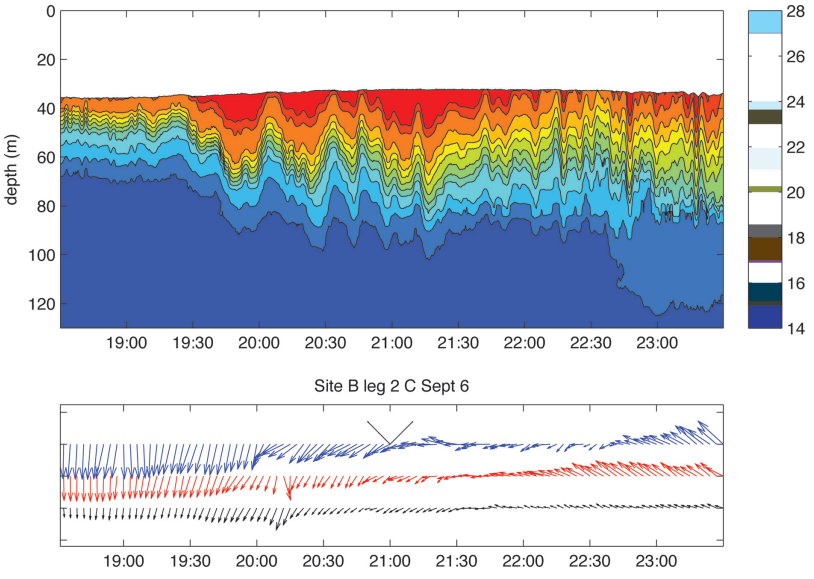

Figure 8. (upper panel) Site B mooring E3 temperature contours. The wave of Figures 6 and 7 may have passed this position at time 22:30; waves can be seen at about this time. (lower panel) Current vectors from near the surface at 36 m depth (blue), a central depth (76 m, red), and near the bottom at 116 m (black) are shown. The shear is evident in the depth dependence. The centered upward arrows sum to one m s^{-1} north (up) for scale (i.e. are each 0.707 m s^{-1}).

to be 0.6 to 1.0 m/s over most of trajectory. Despite the uncertainly of whether the visible waves developed from the measured wave, they are examined here. Waves are most clearly visible to the west of the northern terminus (under the dots). To the east-northeast of the terminus is a faint surface feature that is wider in the across-crest direction than the waves to the west. This feature is somewhat similar to the surface features depicted in two figures of Zhao et al. (2006). Those authors interpreted the features as the surface signatures of large transbasin internal waves of depression expanding in the across-crest direction while moving into shallow water, a process observed with underwater sensors (Orr and Mignerey, 2003; Duda et al., 2004; Duda et al., 2011). Because it is likely that the wave moved slower than 2.0 m/s, a front/wavecrest feature midway along the line that may also mark the eventual fate of the wave is shown with a second row of dots. The refraction to the right of the wave that is consistent with this scenario is a strong possibility in this area of rapid currents. It is also possible that neither feature marked in the figure has evolved from the sonar-imaged wave.

Figure 8 shows Site B mooring data from the same day as the wave encounter. The wave of Figure 6 should have passed by Site B approximately 2.5 hours after the deep-water encounter (22:30 UTC). There are a number of waves evident in the top panel of the figure, one or more of these may have developed from the recorded wave. With no measurements of the wave in the intervening 17 km between the canyon and Site B there is no way to verify

the relationship between the waves at Site B and the wave measured in the canyon, with uncertainty arising in part because waves coming from many directions are found at Site B. Note that Figure 8 also shows strong and variable sheared currents in the area, including strong baroclinic tides and strong surface tides, which can significantly alter the wave speed over the seafloor.

b. Solitary wave modeling

The measurements of the wave made over the canyon are compared to computed solutions of the Dubreil-Jacotin-Long (DJL) nonlinear wave equation (Lamb and Wilkie, 2004; Apel et al., 2007)

$$\nabla^2\zeta + \frac{(N(z-\zeta))^2\zeta}{c^2} = 0, \tag{1}$$

where $\zeta = \zeta(x, z)$ is displacement from vertical position outside the wave and c is wave travel speed (celerity). Solutions to this equation are waves of permanent form, and exist for many wave energies. The purpose of this wave modeling is to find solutions that match the wave observations, and to thus obtain wave parameters such as energy, wave speed and shear from the modeled wave. Boundary conditions are zero displacement at the surface, the seafloor and $|x|$ of infinity. The DJL equation can describe strongly nonlinear waves, and has been chosen because the large maximum displacements of the observed wave, with respect to the depth below the surface of the main thermocline, make weakly nonlinear wave equations such as Korteweg-deVries inappropriate (Apel et al., 2007). An $N(z)$ profile obtained in the area was used to obtain solutions (West Branch North Mien Hua Canyon Station 2 at 25° 26.99′ N, 122° 16.07′ E, water depth 615 m, Sept. 10, 2009 21:08 UTC, Fig. 5). Solutions of (1) were obtained with a code from Frank Henyey (University of Washington) that implements a variational method introduced by Turkington et al., 1991.

c. Analysis of the modeled wave

Note that $\zeta(x, z)$ in (1) is defined such that the process of moving distance ζ vertically from (x, z) places one at the background level z^*, with $N(z^*)$ being the undisturbed stratification profile. Thus, $\zeta(x, z)$ alone does not map streamlines. A simple procedure to map lines having $z - \zeta(x, z) = z^*$ is required to find the streamlines having position z^* outside of the wave. Figures 7 and 9 both show streamlines for a single wave solution that fits the data. Backscatter patterns in Figure 7 line up very well with the model wave streamlines. The maximum shear of the horizontal current ($S = \mathrm{du/dz}$) is found near the level of maximum $N$where is it expected to be, resulting in minimum gradient Richardson number $Ri = N^2/S^2$, overcoming the reducing effect on Ri of low N found elsewhere. The minimum Ri is at 129 m depth in the center of the wave. Backscatter patterns in Figure 7 line up very well with the model wave streamlines. The maximum displacement in the wave is 61 m. The water that achieves maximum displacement resides at about 140 m depth in the center of the wave, having entered the wave at 79 m depth.

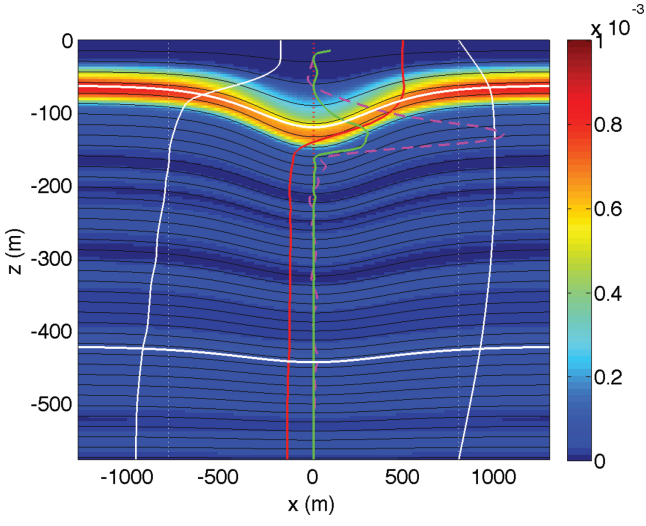

Figure 9. The black lines show streamlines of a solution to the DJL equation. The same solution is depicted in Figure 7. The wave speed is 1.88 m s^{-1}. The colors show $N(x, z)$ in the wave. The scaled velocity profile $u(0, z)$ in the wave center is shown in red; the maximum is 0.99 m s^{-1}. The scaled shear at the wave center is shown with the dashed line; the maximum is 0.026 s^{-1}. A scaled version of the central $Ri^{-1}(0, z)$ profile is shown with the solid green line. The maximum is 1. The upper white line shows $\zeta(x) = A\ \mathrm{sech}^2(x/L)$ with $A = -57$ m and $L = 440$ m for comparison with a nearby streamline. Likewise, the lower white line shows $\zeta(x) = A\ \mathrm{sech}^2(x/L)$ with $A = -22$ m and $L = 580$ m. The linear mode one horizontal current and vertical current function shapes are shown in white at the left and right.

The local available potential energy (APE) of the model wave is 39 MJ m^{-1}. This value of APE per unit crest length of the wave is computed using the Holliday-McIntyre method and is denoted APE$= \int\int \mathrm{APE}_2 dxdz$ in the notation of a recent paper (Kang and Fringer, 2010), where $\mathrm{APE}_2(x, z) = \int_{z-\zeta(x,z)}^{z} g[\rho(x, z) - \rho_r(z')]dz'$ defines the exact local APE density at a given point resulting from the displacement, and where $\rho_r(z)$ is the undisturbed density profile. The depth integration for APE is over the entire water column, and the x integration includes the entire wave. The estimated APE resulting from the constant-N approximation is $\int\int(\rho_0 N^2\zeta^2/2dxdz = 43$ MJ m^{-1}. The kinetic energy (per unit crest length) is defined as $K\tilde{E} = \int\int(\rho_0/2)(u^2 + w^2)dxdz$ and is equal to 48 MJ m^{-1}. The sum of the energies is the pseudoenergy $E = K\tilde{E} +$ APE (Shroyer et al., 2010). For this wave E is 87 MJ m^{-1}, much smaller than the 1800 MJ m^{-1} of one deep-water South China Sea wave measured by Klymak et al. (2006), but far larger than the 7 MJ m^{-1} of the largest wave reported for the Mid Atlantic Bight (Shroyer et al., 2010).

Energy transported onto shelves by large waves of this type is often dissipated in the shelf break region (Orr and Mignerey, 2003; St. Laurent, 2008; Shroyer et al., 2010). This wave has a modeled energy level E that is a factor of 10 (or more) higher than the level that

appears to be sustainable by waves typically encountered on shelves in waters of order 80 m depth (Shroyer et al., 2010). The energy flux of one wave with $E = 8.7 \times 10^7$ passing by per day would be 1.00 kW m^{-1}. A wave with crest length of 40 km would thus transport 40 MW, which is far less than the 9,000 MW estimated to be transported in the central SCS daily by a typical two-wave packet (Klymak et al., 2006), but a significant amount nonetheless. It is anticipated that a large fraction of the energy in this wave will be dissipated in water of depth 300 to 150 m, in processes similar to (but perhaps less dramatic than) those depicted by images of Orr and Mignerey (2003) and Reeder et al. (2008) and quantified by Orr and Mignerey. On the other hand, it may be possible for waves of this energy level to transit onto the shelf somewhat intact, although with steady dissipation along the way. Section 5 describes a wave on the shelf that may have this origin.

Figure 9 also shows two sech-squared streamline shapes. This is the shape of a permanent-form solution to the weakly nonlinear Korteweg-deVries (KdV) wave evolution equation (Lee and Beardsley, 1974; Apel et al., 2007). The similarity of this and the DJL solution suggest that the wave has weak nonlinearity, although the ratio of maximum current u to c is relatively large at 1.00/1.88 = 0.53. Note that the best-fitting sech $^2(x/L)$ shapes have L that are depth dependent, so that the wave differs in shape from KdV equation solutions for mode-one waves that are separable in x and z. Waves analyzed by Vlasenko et al. (2000) also have this nonseparability. The sech-squared wave shape also implies that effects of nonlinearity and nonhydrostatic dispersion are approximately balanced in the wave. Figure 9 also shows the linear mode-one shapes for vertical and horizontal velocities. It has been shown many times that nonlinear waves do not have vertical forms fitting the linear mode shapes (Vlasenko et al., 2005), as seen here. The linear mode-one wave phase speed is 1.46 m s^{-1}, less than the modeled speed of the nonlinear wave, 1.88 m s^{-1}.

The minimum Ri in the modeled (fitted) wave is 1.0, indicating that the wave is stable at this point and not subject to strong shear instabilities often seen in waves of this type (Moum et al., 2003). This is unlikely to remain true as the wave moves into shallow water and the energy density climbs. The stability of the wave is consistent with the relatively gradually sloping bathymetry south of the wave (Fig. 1). The probable path of the wave before the measurement encounter is in water of 700 m to 500 m depth for dozens of kilometers.

d. Observed solitary wave shape

Figure 7 shows a reversal of displacement at the back edge of the wave, at time 1,000 s, depth 70 m (i.e. the isopycnals rise above their observed equilibrium positions prior to the wave arrival). This is also called a kink in the terminology of Yang et al. (2004). This instability is expected for the shoaling bathymetry of the site, diagrammed in Figure 1. The shape is reminiscent of computed behavior of disequilibrium wave shapes evolving toward equilibrium (Vlasenko et al., 2005, Chapter 5).

There is a little evidence in Figure 7 of the now familiar highly deformed inclined-plane leading edge of the wave (ramp shape). However, the kink appears to accompany a slight

steepening of the trailing edge. This steepened shape can appear in waves encountering the critical zone where $h_1 = h_2$ (Grimshaw et al., 1999) and where waves encounter shallow water, found in numerical studies (Vlasenko and Hutter, 2002; Vlasenko et al., 2005) and in nature (Orr and Mignerey, 2003; Duda et al., 2004; Scotti et al., 2008; Reeder et al., 2008). The only slight deformation of this particular wave is consistent with this wave having a smaller ratio of maximum displacement to water depth than the previously observed deformed waves.

e. Solitary wave formation from an internal tide

The wave analyzed in the previous section is highly likely to have evolved from internal tides generated near the Ilan Ridge to the south. A scenario like this has been observed in the Luzon Strait area south of Taiwan and was analyzed in terms of the interplay of nonhydrostatic dispersion, nonlinear steepening and rotation (Li and Farmer, 2011). In this section, the tidal forcing at Ilan Ridge is discussed, relevant recent wave evolution work spread over a few papers is reviewed, and the scaling arguments governing the evolution of disturbances originating at the Luzon Strait and Ilan Ridge are compared.

The barotropic M_2 (12.42 hr period) tidal ellipses shown in Figure 3 illustrate that the strongest currents at the ridge are meridional, and normal to the ridge crest, which is a favorable situation for internal tide generation. The ellipses in the Ilan Ridge area have major axis lengths less than 20 cm s^{-1} except at a few island passages, The densimetric Froude number $Fr = U_0/(g'D)^{1/2}$ (Turner, 1973) can be used to analyze mode-one internal tide generation. In the definition, $g' = g(\rho_2 - \rho_1)/\rho_2$ is reduced gravity, U_0 is the current speed, and D is the vertical length scale of the shear zone, while $\rho_2(\rho_1)$ is the lower (upper) layer density, and g is gravitational acceleration. This is (essentially) the Froude number for the mode-one baroclinic wave, $Fr_n = U_0/c_1$ where c_n is the phase speed of the mode-one wave. For velocities in Figure 3, Fr is subcritical (less than one) over most of the ridge. For example, with $U_0 = 50$ cm s^{-1}, $(\rho_2 - \rho_1) = 3.5$ kg m^{-3}, and $D = 200$ m, Fr would be 0.2. In the subcritical case, long-wavelength internal tides are likely to be formed over most of the ridge, with the possible addition of some localized nonlinear waves or lee waves where the U_0 are higher. Conditions at the eastern ridge of the Luzon Strait are also subcritical (Li and Farmer, 2011).

A suitable equation for analyzing internal tide modal evolution is the rotationally modified extended Korteweg deVries (KdV) equation (Holloway et al., 1999)

$$\frac{\partial}{\partial x}\left(\frac{\partial \eta}{\partial t} + c\frac{\partial \eta}{\partial x} + \alpha\eta\frac{\partial \eta}{\partial x} + \alpha_1\eta^2\frac{\partial \eta}{\partial x} + \beta\frac{\partial^3 \eta}{\partial x^3}\right) = \gamma\eta, \tag{2}$$

where $\gamma = f^2/2c$ (units m^{-1} s^{-1}), f is the Coriolis parameter, c is linear phase speed for the wave mode being analyzed (baroclinic modes in our case), η is the normal mode amplitude, the α are modal coefficients of nonlinearity, and β is the mode coefficient of nonhydrostatic dispersion. The interplay of nonlinearity, nonhydrostatic dispersion and

rotation in the evolution process has been studied by Li and Farmer (2011, LF11) using the similar Ostrovsky equation (rotationally modified KdV eq.) (Apel et al., 2007), which neglects the cubic nonlinear term.

LF11 observed that nonlinear waves formed after internal tides propagated more than 180 km westward from their surmised Luzon Strait generation site. Their analysis of the Ostrovsky equation supported 180 km as the distance required to form nonlinear waves from the semidiurnal internal tide. On the contrary, the nonlinear wave analyzed here in sections 4a-4d was only about 100 km north of Ilan Ridge, indicating differences in the scaling for the two sites. Importantly, the South China Sea waves propagate in water having relatively uniform depth 2,500 m (with the exception of the narrow ridge which they pass over), whereas the wave analyzed here has apparently formed from internal tides propagating briefly in water of 1,500 to 2,000 m depth but then moving into shallow water. The internal tide amplitudes may also differ at the two sites, but the Ilan Ridge internal tide amplitude has not been confirmed.

The LF11 analysis for the Luzon area employs a two-layer approximation. That paper shows, using two parameters, that sizable interface waves are expected to steepen because of nonlinearity, with rotation inhibiting but not preventing this. The parameters are the Ursell number and the Ostrovsky number, which are ratios of nonlinearity to nonhydrostatic dispersion, and nonlinearity to rotation effect, respectively. For the two-layer system these are given by

$$U_r = \frac{AL^2|h_1 - h_2|}{h_1^2 h_2^2}, \tag{3}$$

and

$$Os = 12\pi^2 \frac{\alpha A}{\gamma L^2} = \frac{36\pi^2 A g' |h_1 - h_2|}{f^2 \lambda^2 (h_1 + h_2)}. \tag{4}$$

Here, A is the wave amplitude, L is horizontal length scale, h_1 and h_2 are upper and lower layer thicknesses, and λ is wavelength. The factor $12\pi^2$ makes $Os = 1$ the transition point (critical point) between breaking or non-breaking internal tide, discussed in the next paragraph. Analysis of Ur for the internal tide indicates that nonhydrostatic dispersion (the β term) can be dropped from the Ostrovsky equation up until the point that solitary waves are formed. Dropping this term and invoking a Galilean transformation (variable change $\hat{x} = x - ct$, $\hat{t} = t$), yields the Ostrovsky-Hunter equation (OHE, Boyd, 2005), which is a modified shock wave equation suitable for nonlinear internal tides with hydrostatic pressure, and which exhibits a reduced number of possible term balances:

$$\frac{\partial}{\partial \hat{x}} \left(\frac{\partial \eta}{\partial \hat{t}} + \alpha \eta \frac{\partial \eta}{\partial \hat{x}} \right) = \gamma \eta. \tag{5}$$

The parameter Os controls steepening behavior in (5) and often in (2). For stable water depth and stratification, Os evolves as the internal tide propagates primarily because nonlinear steepening reduces the scale L. For the OHE, regime $Os < 1$ lacks steepening (wave

breaking), regime $1 < Os < 2$ is where rotation inhibits steepening, and regime $Os > 2$ shows steepening unmodified by rotation. The LF11 analysis equates steepening to a regime where nonhydrostatic pressure is no longer negligible (i.e. to a regime where internal solitary waves such as the wave observed by *RV OR1* can form), and the applicability of (5) expires. LF11 found normalized breaking times t_b of approximately 1.5 and 1.0 for fixed *Os* of 2.0 and 3.0, respectively. With normalized (but dimensional) breaking time defined by $t_b = t\gamma^{1/2}$, these t_b convert to t of 0.73 days and 0.48 days, respectively, using $c = 2.5$ m s^{-1} and $\gamma^{1/2} = 2.4\times10^{-5}$ at the Luzon Strait latitude. The distances covered by waves of this speed in these times are 158 and 103 km, respectively, with the former being close to the observed breaking distance of 180 km. In summary, an *Os* value of 2.0 is consistent with South China Sea semidiurnal internal tides, and the theory fits well with the observed 180 km transition scale.

Given sufficient information to assess *Os* in the area between Ilan Ridge and QPE, the LF11 methodology could be applied there. However, the required A, h_1, h_2 and L are poorly characterized at this time. Also, the encounter of the QPE internal tide with the continental slope implies a much stronger time dependence of *Os*, thus complicating the characterization of steepening behavior (the parameter governing the evolution time scale is, itself, changing). Applying the method nonetheless, a more rapid formation of nonlinear waves north of Ilan Ridge than west of Luzon Strait implies a higher *Os* north of Ilan. A 100 km transition scale implies $t < 11.1$ hr at $c = 2.5$ m s^{-1}. At latitude 25° this implies $t_b < 0.95$, which is consistent with the breaking time for *Os*~3 or higher. This *Os* ratio of 3/2 for semidiurnal internal tides at the two locations has many possible explanations. North of Ilan Ridge, either 1) A can be greater; 2) $|h_1 - h_2|$ can be greater (unlikely, the opposite is expected); 3) λ can be reduced (this is probable based on internal tide modal dispersion analysis); or 4) the average water depth $(h_1 + h_2)$ can be less. (The depth is less, of course, in the shoaling area 100 km north of Ilan Ridge). The large number of parameters allows many possible explanations for differences between Luzon Strait and QPE *Os* values. One simple way for the breaking distance to drop to half the Luzon Strait value of 180 km would be to keep all of the parameters the same except for the water depth, (with h_1/h_2 adjusting so that $|h_1 - h_2|$ is constant). Also, one may expect A to increase over time in the QPE situation, as the wave is confined to a shallower waveguide. Thus, depth and amplitude parameter differences between the QPE and Luzon Strait sites form a reasonable explanation for the early appearance of the moderately sized QPE transbasin internal solitary wave. To move beyond this speculation, better measurements in the area north of Ilan Ridge are required to constrain *Os*, or alternatively to provide information needed to perform a fully nonlinear wave breaking analysis as employed by Li and Farmer (2011). Also, note the scaling analyses above neglect the effects of sheared background flow on the steepening process, although shear is likely to play a role in the Kuroshio north of Ilan Ridge.

Another candidate method to explain the difference between Luzon Strait and QPE, would be analysis of the full equation, (2), including the cubic nonlinear term. Using the Station

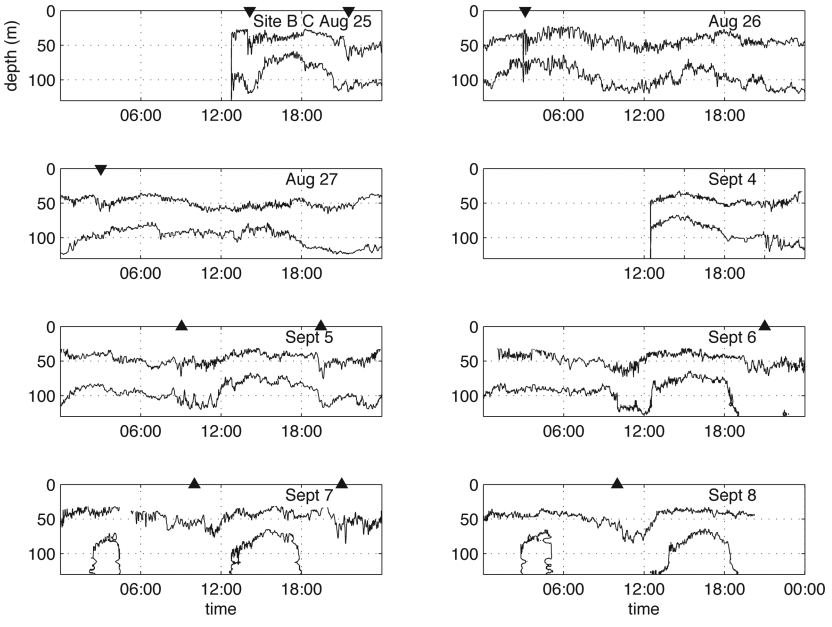

Figure 10. The 23° and 16.5° C isotherms at Site B mooring E3 are plotted for the durations of the two deployments. The 10 triangle symbols at the top indicate beginnings of time intervals of increased nonlinear internal wave activity. The occasional multiple values (in depth) of the deep isotherm indicate salinity intrusions.

2 profile of Figure 5, and assuming a small density gradient deeper than 600 m depth, the ratio of the nonlinear terms $(\alpha_1\eta/\alpha)$ along a transect from Ilan Ridge to the canyon site can rise to 0.2 for $\eta = 10$ m or to 0.4 for $\eta = 20$ m. These values imply that the cubic term may indeed play a role, and breaking analysis using only the OHE may be insufficient. Preliminary analysis of wave evolution via solution of (2) yields results consistent with the appearance of the Sept. 6 wave, but reporting this computation in detail is beyond the scope of this paper.

5. On-shelf nonlinear wave properties

Measurements of shelf internal waves in water shallower than 150 m with the Sites A and B moorings and the ship systems are reported in this section. Figure 10 shows time series of two isotherm depths measured by Site B mooring E3. These two isotherms are accurately mapped because the mooring had 21 sensors between 30 and 125 m depth. The windows are each one-day in length. The oscillations of the deep (16.5° C) isotherm mainly show the internal tide response. The shallow (23° C) isotherm shows the internal tide and the nonlinear internal waves. The deep isotherm sometimes disappears because of lateral

advection. Ten time windows of strong nonlinear wave activity are marked with triangles. The waves with the largest vertical displacements occur in the first, third and ninth windows.

Contour plots of isotherms for the 10 windows are shown in Figure 11. The sensor positions are shown in Figure 12. Isotherms deeper than 30 m are well mapped by the dense array of sensors. Figure 11 shows the wave packet structures to be highly variable. The first packet, for example, is roughly rank-ordered by amplitude and short lived. The third packet is rank-ordered at the start, like the first, but continues for many hours. With the fishing destruction of the other two Site B moorings, and with no fast-sampling ADCP, the propagation directions of many of these passing waves are not known. It is quite possible that there is more than one packet of waves passing by at any given time, in multiple directions (see Fig. 2). The ship's radar images show that waves moving in many directions inhabited the area.

The distribution of internal wave directions near site B was found using data from the unaliased SW-B ADCP and the employment of a variation of the methods used by Ramp et al. (2004) to find wave directions in the South China Sea. The (u, v) record (east and north velocity) from 65 m depth was high-pass filtered, allowing signals with frequency greater than one cycle per five hours to pass. A time series with no gaps from 1600 UTC Aug. 22 to 0500 UTC Aug. 31 was used. Peak speeds in this record were identified as being caused by internal waves. The current vectors of the peaks are shown in Figure 13. The upper left shows peaks greater that 0.35 m s^{-1} (quantity 167, about 20 per day), the lower left shows the subset (quantity four) with peak speeds exceeding 0.7 m s^{-1}. The upper-level high-pass currents are closely aligned with the wave direction. On the right, the histogram of peak 65 m current direction (wave direction) is shown for each group. Many waves are found to travel to the southeast, which is consistent with Figure 2, as well as to the northwest. Large waves with high speeds are found traveling north (see Section 4), east and southeast. The radar images and the SW-B ADCP record shows many waves traveling in a variety of directions. The short period of the field effort, and the wide-ranging ship track, makes this survey of wave directions less than comprehensive.

The Site B wave with the highest measured amplitude lies in the third window (Figure 11, Aug. 26). A wave that is almost as large appeared in window 9 (Sept. 6). The Aug. 26 wave packet is plotted in more detail in Figure 12. This wave had maximum displacement of about 36 m, which is 28% of the water depth. If one takes 35 m as the depth of the main thermocline prior to the wave (this estimate has large error bars of $\pm 10\%$ because of the lack of sensors between 30 and 1 m depth), then the ratio of the displacement to the depth of the upper layer in a comparable two-layer system is near one. This ratio is one measure of wave nonlinearity, and the value indicates that the wave is not weakly nonlinear.

The Aug. 26 wave packet (Figs. 11 and 12) was also measured with the SW-B ADCP in about 140 m water depth. Figure 14a shows east, north and upward velocities (u, v, w). A MODIS satellite image for this time depicts a wave packet with a very long crest (Fig. 14b). The shape, with the long crest, does not follow the bathymetry, implying that this is a transbasin wave packet. The wave packet may form via breaking of the internal tide after

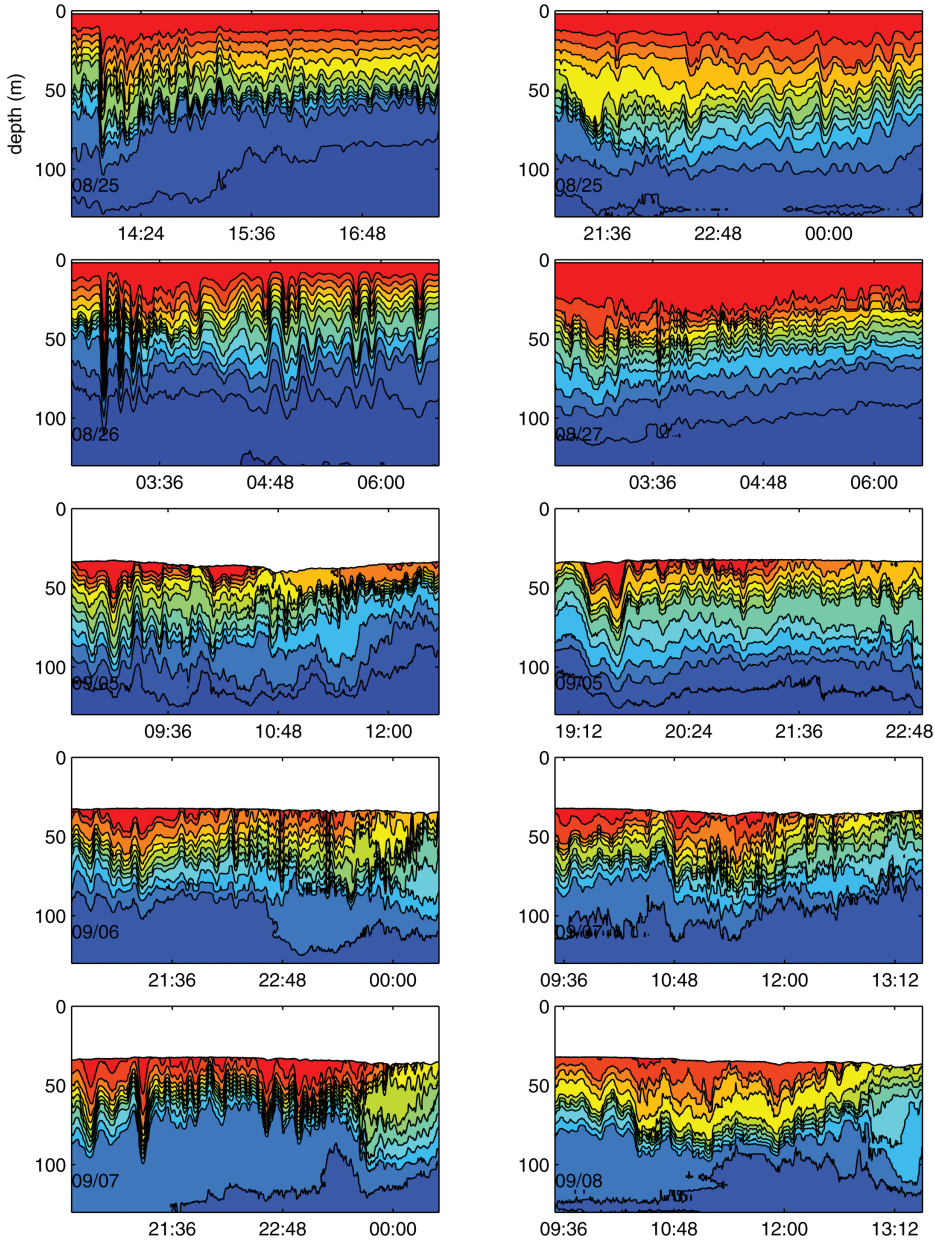

Figure 11. Isotherm contours from Site B mooring E3 are shown for the 10 intervals of active nonlinear internal waves. The contours interval is 1° C, 14 to 28. These are the 10 four-hour windows indicated with symbols in Figure 10. The dates for each frame are indicated. Time advances from upper left to lower right as in Figure 10. The plotted depth range is very close to the water depth.

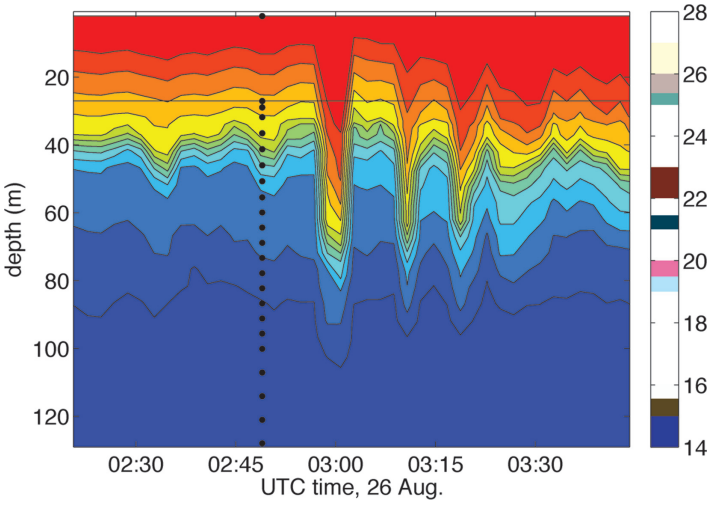

Figure 12. A contour plot of the largest wave recorded by the moorings is shown. The data are from Site B mooring E3, leg 1. This wave was also measured with Seasoar. The dots show the median depth positions of the sensors. Contours below the line at $z = 27$ m are mapped the best; above the line the contours are interpolated with greater uncertainty. The mooring was also in position during leg 2 but had no surface sensor, to explain the data coverage differences in the Figure 11 plots. The one-minute sampling rate of the lowest-rate sensors on this mooring barely resolves the waves.

attaining high *Os* in fairly deep water as explained in Section 4e. However, because the wave is not seen in deep water, it can't be verified with certainty that it is a transbasin wave. Another interpretation is that this wave packet formed in shallow water from a long-wavelength transbasin internal tide wave less strong than the one assumed to spawn the Sept. 6 wave directly observed in deep water (Section 4). This weaker internal tide wave may have reached the "breaking point" only after reaching the shelf, creating waves weaker (fewer MJ m^{-1}) than the Sept. 6 wave. With this limited data set it is not possible to determine whether this packet evolved from a transbasin internal tide, evolved from a transbasin nonlinear wave, was generated locally from a locally-generated internal tide, or was generated by local supercritical flow over a slope.

The Aug. 26 wave packet was also measured at a position north of Site B by radar image, echo sounder, and Seasoar undulating CTD (Chelsea Technologies, Surrey, UK) towed behind *OR1*. These measurements were made at 122° 36.816′ E, 25° 44.98′ N at 04:11 UTC. This is 5.43 km north of the Site B E3 mooring at heading 354.7°, indicating a wave speed of 1.27 m s^{-1} along that track. (The wave must have been advected by the sheared currents because the speed of the fitted nonlinear wave is 0.86 m s^{-1}, and the calculated linear mode-one wave speed is 0.76 m s^{-1}.) Only one large wave was present, so the packet evolved. The radar image of the wave (Fig. 15a) shows a much narrower rough band than the offshore wave (Figs. 6 and 7). The wave appears to be heading at 3°, so the speed of the

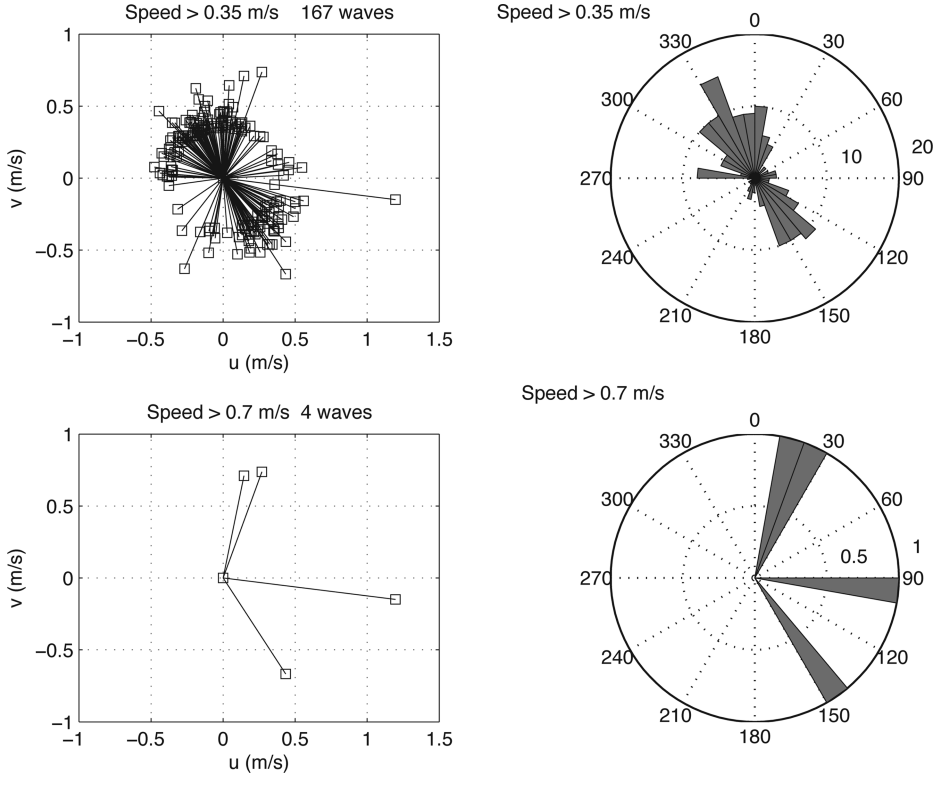

Figure 13. Peak current vectors at 64-m depth, taken from the SW-B ADCP record, for identified above-threshold events (internal waves), are plotted on the left. Two speed thresholds of 0.35 (top) and 0.7 m s^{-1} (bottom) were used. On the right are histograms of the wave directions, in 10° bins, for the two sets of events.

wave normal to its crest is slightly less, 1.26 m s^{-1}. The transect of Seasoar data shows the packet at position 8 km (arbitrary scale), although the sampling does not fully resolve the individual waves (Fig. 15b).

Using the speed information from the ship/wave encounter, the x-axis of Figure 12 can be converted to meters. Fitting sech-squared weakly-nonlinear (KdV) wave shapes to the wave in this coordinate frame suggest that $\mathrm{sech}^2(x/L)$ with $L = 190$ m fits reasonably well. However, the wave appears flat-bottomed, as do highly nonlinear waves of ASIAEX-SCS (Duda et al., 2004) and theory (Helfrich and Grimshaw, 2006). In fact, a scaled plot of this wave looks eerily similar to the 160 m displacement internal wave plotted in those two papers. Note that another wave headed at approximately 355° followed four minutes after the large wave, barely visible in Figure 15a. The appearance of these two waves together is in striking contrast to the lack of waves in images for hours before and after, motivates

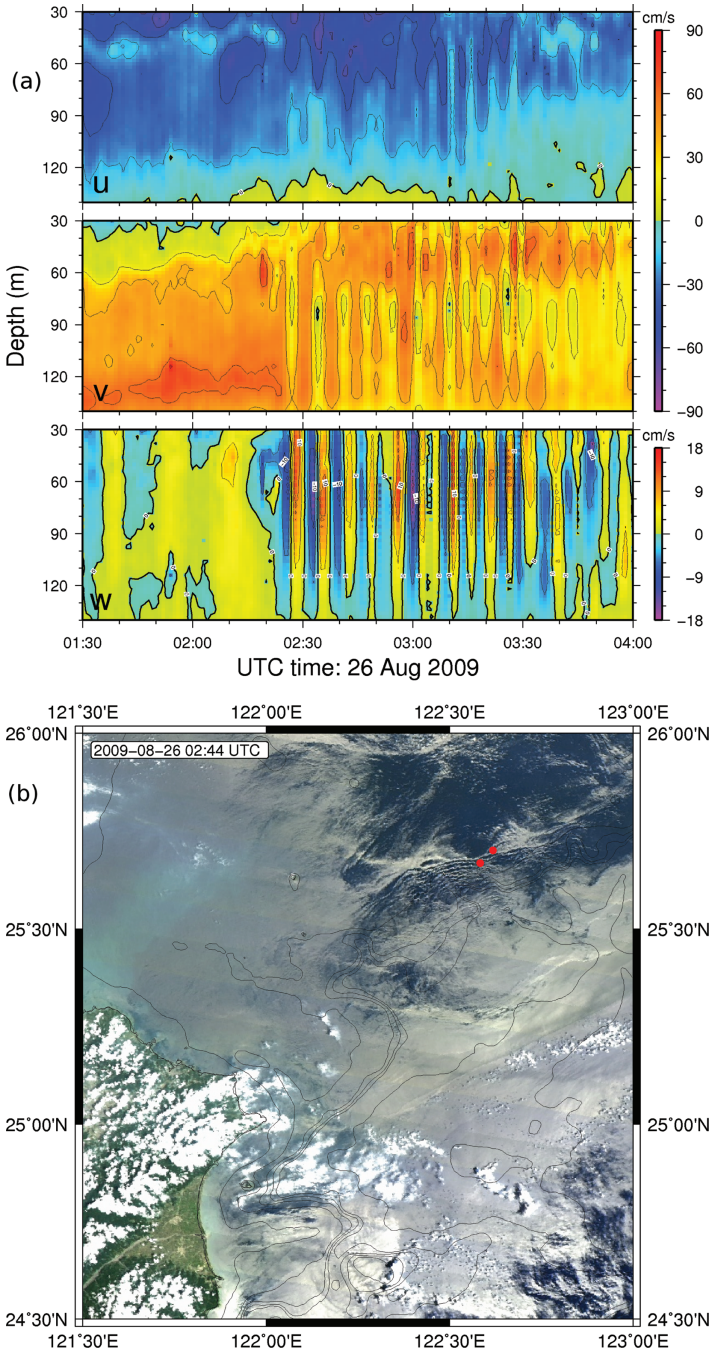

Figure 14. (a) From top, eastward, northward and upward velocities are plotted, measured at the SW-B ADCP. The waves are likely those seen at Site B (Fig. 12), arriving here slightly sooner. (b) A MODIS image likely shows the waves depicted in Figures 12 and in (a) above. The dots show the locations of the SW-B ADCP (left) and Site B (right).

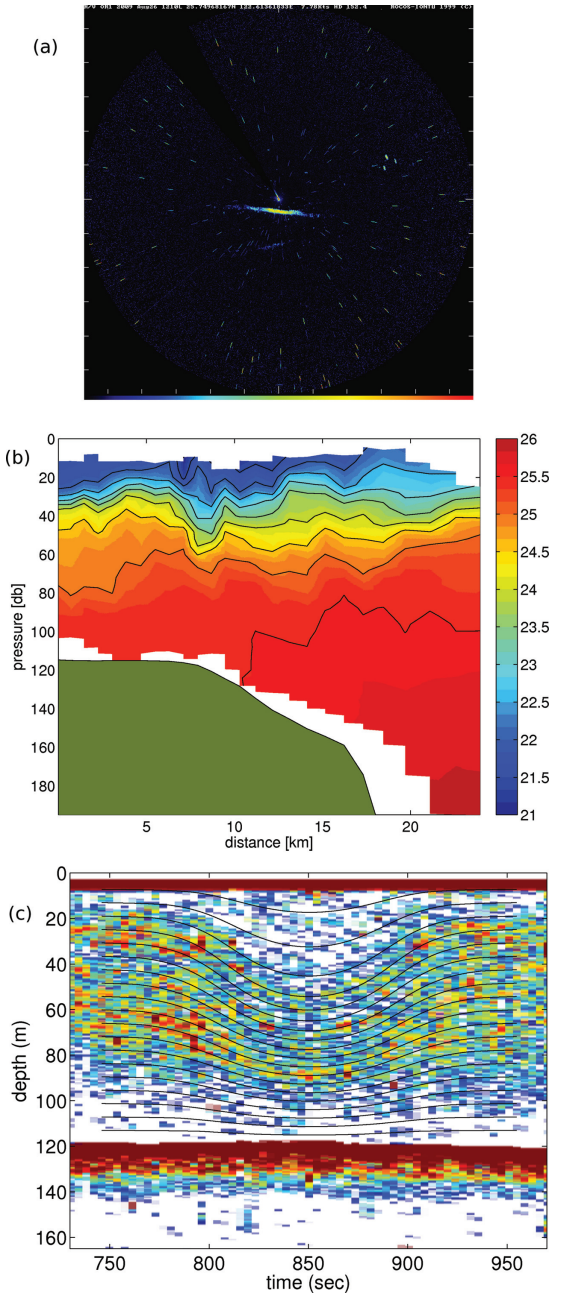

Figure 15. The ship's radar image is shown in original format for the wave encountered near the Site B moorings. This wave is also visible in the EK500 sonar data. The ship was moving to the south at a position north of Site B. This position is marked with a circle in Figure 1. The scale is the same as for Figure 6. (b) A Seasoar potential density section is shown in color; the location appears in Figure 1. A wave packet is visible at position 8 km. Black contours are 21.5 to 25.5 kg m^{-3} by 0.5. (c) The EK500 image of the wave is shown. Streamlines of a solution wave of the DJL equation are also drawn. The fit of the computed wave to the data has not been optimized. APE for the computed wave is 7.1 MJ m^{-1}. The streamlines are 1,000 m in length.

the speculation that these waves are not fully independent, and may have evolved from the same source feature (e.g. internal tide or transbasin wave).

A computed DJL wave shape (not shown) that roughly fits the large wave at the mooring (Fig. 12) has APE 8.7 MJ m^{-1}. (The modeling method Section 4b was used.) This waveform was computed using a Seasoar density profile taken just prior to the wave encounter, with maximum $N(z)$ of 22.6 cph (Fig. 5). Maximum displacement in this wave is 34 m. Minimum Ri in the main thermocline was 1/20, indicating a high propensity for shear instability, and a likelihood that the wave was losing energy to shear-induced turbulence when observed. A slightly smaller version of this wave was computed to fit the echo sounder image of the wave (taken at 04:11 UTC north of the mooring), and is plotted in Figure 15c on the echogram. This wave has maximum displacement 29.7 m and APE = 7.1 MJ m^{-1}, at water depth 119 m.

6. Internal tide on the shelf

The Site A and Site B ADCP's measured velocity over approximately 65% of the water column for a few weeks, and were able to capture some aspects of the internal tide currents. Without adjacent continuous measurements of stratification, the commonly measured quantity of baroclinic wave energy flux $\bar{u}' p'$ was not measured, with $\bar{u}'$ being wave horizontal velocity vector and p' being wave perturbation pressure. However, the ADCP's do allow for comparison of tidal band wave kinetic energy (KE) with other areas and with model predictions. Initially, the velocities were band pass filtered to extract the tidal signals. High-order lowpass Butterworth filters were applied at each edge of the band. These were each applied twice, once in each direction, to eliminate phase shifts. The low cutoff filter was fourth order, the high cutoff filter was eighth order. The response of the dual filtering was −20 dB at the band edges of 0.3 and 2.8 cycles per day. Spectra of the raw and filtered timeseries are shown in Figure 16. Next, the currents were depth averaged to obtain the barotropic tide estimate (U, V) for each site. The residual after subtracting this formed the baroclinic tide estimate. To test whether this procedure was reasonable, (U, V) for each site was treated with tidal harmonic analysis, and the difference between the barotropic tide estimate and the TPXO prediction for each site was analyzed. The tidal ellipses fit the local tidal inverse model predictions (Egbert and Erofeeva, 2002) reasonably well. Estimated and inverse model predicted tidal constituent M_2 ellipses are shown in Figure 17. The Site B prediction has rms current speed 44 cm s^{-1}, with residual speed (prediction minus (U, V)) of 12 cm s^{-1}, and with 92. 6% of the variance of the prediction fitted by (U, V). For Site A, these values are 38 cm s^{-1}, 9 cm s^{-1}, and 94.4%, respectively. The baroclinic and barotropic tidal band velocity time series were further filtered and divided into semidiurnal species and diurnal species components. An eighth order low-pass Butterworth filter was used, applied twice, as with the tide bandpass filtering. The separation of the tidal species was 15 dB at the crossover (1.5 cpd) and exceeded 30 dB at the center of each species band. The baroclinic tidal band velocities (both species together) at Site A are shown in Figure 18.

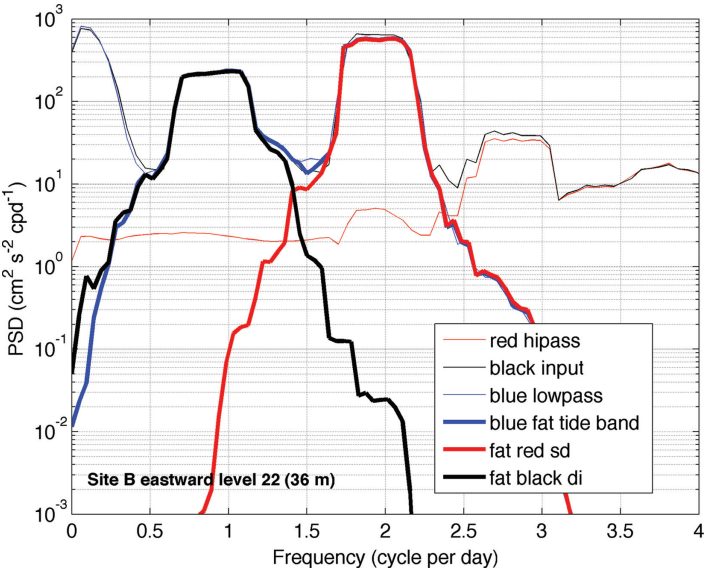

Figure 16. Spectra of unfiltered and filtered versions of one ADCP time series are shown. The three thick lines show the diurnal band, the semidiurnal band, and the total tidal band spectra. The thin lines show the spectra of the total (input) signal, the supertidal highpass filtered signal, and one lowpass (tidal and subtidal) band signal. The subtidal spectrum is not shown, but can be inferred.

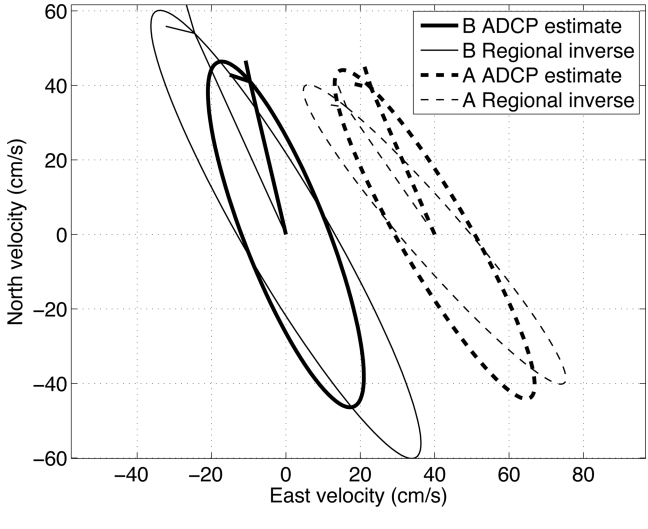

Figure 17. The Sites A and B ADCP-estimated M_2 barotropic tidal current ellipses are shown. These are similar to the published regional inverse ellipses, also shown.

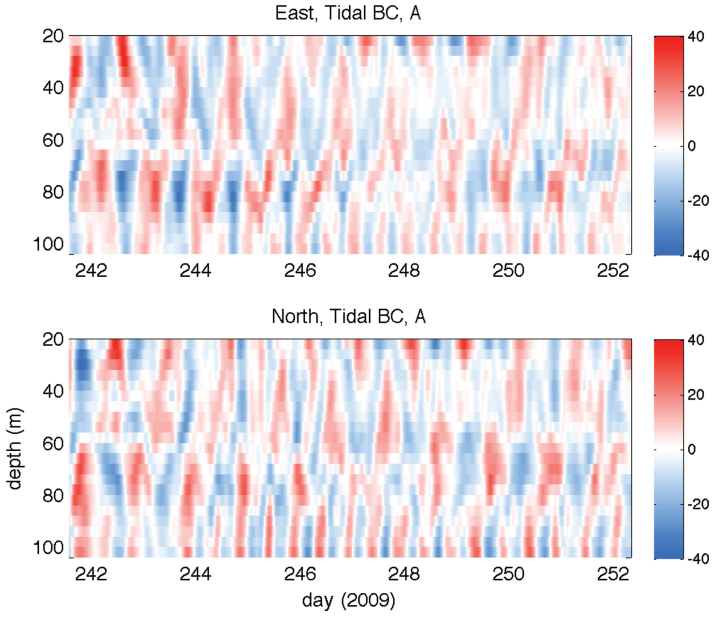

Figure 18. Time series of baroclinic tidal velocity vectors at Site A are shown in color. The east component is shown at the top, the north component below. Units are cm s^{-1}.

An accessible statistic of tidal wave strength is the KE density $E_k = \langle \frac{1}{2}\rho_0(u^2 + v^2 + w^2)\rangle \approx \langle \frac{1}{2}\rho_0(u^2 + v^2)\rangle$. Disregarding the small vertical velocity w and integrating this with depth yields energy per unit area, units J m^{-2}. Energy of the internal waves is a quantity related closely to acoustic scattering behavior (anomalous acoustic propagation), and is of interest because it is closely related to acoustic scattering behavior (anomalous acoustic propagation), as well as being accessible from the measurements. Table 2 shows the time average of depth-integrated KE for both types of tidal waves and both species, with similar entries for other locations included for comparison. (The numbers were scaled upward by F^{-1} to form depth-average estimates for the entire water column, where F is the fraction of the water column sensed by the ADCP. All entries in the table are from ADCP records and are processed with the same code. Note that the barotropic values in the table are representative only (they are not derived using tidal analysis), and the baroclinic values are for the tidal species bands, and are also not derived using tidal analysis.) The energy of the semidiurnal barotropic tide is by far the largest at the QPE sites. However, the QPE baroclinic semidiurnal energies are weaker than values suggested by plots appearing in Niwa and Hibiya (2004). Nonetheless, these levels exceed by a factor of 10 the levels found at three shelf locations selected for comparison, the locations being the New Jersey shelf site of the SW06 experiment (Newhall et al., 2007), the central coast of Maine and a site east of northern Florida (Nash et al. 2012). The QPE baroclinic semidiurnal energies are comparable

Table 2. Estimated average kinetic energies of QPE barotropic and baroclinic tides. Units J m^{-2}. Estimates from additional areas are given for comparison. The ASIAEX South China Sea (SCS) baroclinic values are from Duda and Rainville (2008), the others were computed from ADCP records. Summer stratified time periods are used for the non-QPE data sets. Diurnal estimates are not given for locations where this frequency band is subinertial. The Malin Shelf and NDBC data are further described by Nash et al. (2012).

Station identifier	*Water depth*	*Barotropic semidiurnal*	*Barotropic diurnal*	*Baroclinic semidiurnal*	*Baroclinic diurnal*
QPE Site B	134 m	9,800	410	370	740
QPE Site A	112 m	8,600	210	190	680
SW06 SW30	81 m	310	–	30	–
ASIAEX-SCS S4	120 m	380	1780	280	1,880
Malin Shelf[a]	147 m	1,380	–	250	–
NDBC 41012[b]	37 m	450	–	40	–
NDBC 44032[c]	100 m	180	–	40	–

[a]Malin Shelf: May 5, 1995-July 30, 1995. 56.467° N, 8.967° W.
[b]NDBC Station 41012: May 30, 2006-Aug. 22, 2006. 30.042° N, 80.534° W. St. Augustine, FL.
[c]NDBC Station 44032: June 25, 2007-Aug. 1, 2006. 43.715° N, 69.358° W. NERACOOS Central.

to those found in ASIAEX-SCS, with both experiments showing less baroclinic semidiurnal KE in shallower water than in deeper water (not shown here for ASIAEX), suggestive of dissipation. The high semidiurnal baroclinic KE values of QPE and ASIAEX are not unique, with Table 2 showing a similar high value for the Malin Shelf west of Scotland, UK (Small et al., 1999). Additionally, the QPE sites show strong baroclinic diurnal internal tide KE, exceeding the KE in the diurnal barotropic tides. These large baroclinic diurnal energies may have an origin at a critical slope, similar to what is suggested by Duda and Rainville (2008) for the large ASIAEX baroclinic diurnal waves. The energy flux $E_k c_g$ of the internal tides, where c_g is the group velocity, can be estimated assuming equipartition of energy. For the baroclinic semidiurnal tide at Site B, $370 \times 2 \times 1.0\ \mathrm{m\ s^{-1}} = 740\ \mathrm{W\ m^{-1}}$, comparable to the estimated nonlinear wave energy flux (Sec. 4c), as is typical. (Note that the energy flux of the barotropic tide generally far exceeds that of the baroclinic tide because the barotropic group velocities c_g are so large.)

The KE of the surface tidal and internal tidal currents can be compared to that of other currents in the area. The tidal band currents have six times the KE of the currents at frequencies greater than 2.5 cpd, which includes the currents of the nonlinear waves, some of which are attenuated via three-minute sampling (Site A and B ADCPs). The tidal band currents contain 78% of the total energy, and the high-frequency currents contain 15% of the energy, leaving 7% in the subtidal band (which by convention does not include the mean currents).

The tidal band current speeds measured by the instruments are quite large and often approach or exceed the linear mode-one baroclinic wave speed, making the Froude number

Table 3. Speed statistics (cm s^{-1}) of various current time series for Sites A and B ADCPs. For the barotropic time series the flows exceeding the 95% quantile are cross-slope directed.

Current time series	*Mean speed*	*Median speed*	*95% quantile speed*	*RMS cross-slope*	*RMS along-slope*
B tidal band and subtidal, $z = 36$ m	45.7	46.2	87.5	45.3	19.2
B tidal band, $z = 36$ m (z of max. mean speed)	43.0	42.1	79.0	44.9	15.9
B barotropic	35.3	32.4	66.0	38.2	10.0
B barotropic semidi. (sd)	34.1	31.7	63.2	37.0	8.9
B barotropic diurnal (di)	6.9	6.2	15.1	6.4	4.5
B baroclinic $z = 36$ m	15.6	15.1	29.2	13.4	11.2
B baroclinic sd $z = 36$ m	9.5	9.1	18.0	9.0	7.0
B baroclinic di $z = 36$ m	12.7	12.9	21.3	10.6	8.4
A tidal band and subtidal, $z = 92$ m	40.6	39.5	71.3	41.9	12.4
A tidal band, $z = 92$ m (z of maximum mean speed)	39.2	38.7	69.0	42.0	11.2
A barotropic	35.6	35.2	63.6	38.1	11.0
A barotropic sd	35.0	34.2	62.6	37.5	10.5
A barotropic di	5.4	5.3	9.8	5.4	2.8
A baroclinic $z = 20$ m	16.1	14.5	33.3	12.9	13.4
A baroclinic sd $z = 20$ m	6.1	5.5	12.8	4.0	5.6
A baroclinic di $z = 20$ m	14.2	10.8	30.6	12.0	11.9

near-critical or critical and likely causing localized nonlinear wave phenomena (Vlasenko et al., 2005). A representative shelf-break mode one phase speed computed via truncation of the deep Station 2 $N(z)$ profile at 150 m depth is $c = 1.00$ m s^{-1}. Recall that the speed computed for the location north of Site B of $c = 0.76$ m s^{-1}. Table 3 contains statistics of tidal band current speeds in the area for total signals and separated barotropic, baroclinic, semidiurnal (sd) and diurnal (di) signals. The 95% quantile speeds approach the representative C values at each site.

Finally, there are some interesting depth structures in the Site A baroclinic tidal currents shown in Figure 18. There is a strong diurnal dominance at shallow depth, particularly late in the record. Figure 19 shows line plots of the currents at two depths. The diurnal internal tide at 20 m depth gradually disappears with depth, suggesting a large number of modes are present, which is consistent with a vertically propagating beam of energy, possibly similar to that seen in deep water to the south (Lien et al., 2013). The large diurnal internal tides (Table 2 and Fig. 19) and their possible beam-like nature suggest a process of baroclinic tide generation at a gradual slope of large area (present south of Site B) like that postulated by Duda and Rainville (2008) to occur in the ASIAEX-SCS area.

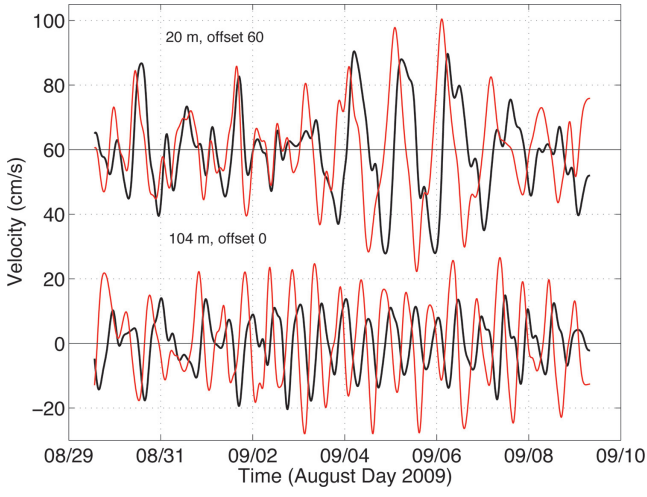

Figure 19. Time series of velocity at two depths at Site A, 20 m (top) and 104 m (below). The data are extracted from the dataset of Figure 18. The thin red lines show the north current, and the thick black lines show the east current.

7. Summary

Many characteristics of internal waves and internal tides were measured in the QPE study area east-northeast of Taiwan. Many aspects of the data collection were not optimized for internal wave studies, but many interesting internal wave features were observed nonetheless.

First of all, a large transbasin wave was observed in deep water, moving into the area from the south (Section 4). The wave may have formed from internal tides generated at the Ilan Ridge 100 km to the south. If so, the wave formed more quickly than similar waves in the Luzon Strait area. This wave was also less energetic than the large waves generated at Luzon Strait. A rationale to explain the formation was presented. The wave was analyzed in detail by comparing it to a well-fitting solution to the DJL equation and was found to be consistent with a stable highly nonlinear wave of permanent form, with the energy of the wave and the flow field within the wave analyzed in some detail.

Next, the nonlinear internal wave conditions on the shelf over a seven-day period (composed of two shorter periods, with a gap) were examined with mooring data. Wave conditions were found to vary over time in many respects, and the day-to-day resemblance of wave conditions was quite small. One large wave was measured by a mooring and by shipboard sensors, having approximately 34 m maximum displacement. The measurements allowed proper constraint of DJL-equation modeling of the wave. The wave was found to be highly nonlinear and likely to spawn shear instability in the main thermocline. This wave had 10% of the energy of the deep-water wave. The modeled wave was 10 to 15 times more energetic than similar waves measured east of the United States at the SW06 site. It could not be determined whether this wave evolved from a wave like the deepwater wave analyzed in

Section 4, or was spawned locally. The large size of the wave could be due to the large energy of its probable source, an energetic transbasin wave or wave packet, or alternatively, due to being derived from local internal tides that are much stronger than the SW06 internal tides. There was no in situ evidence that transbasin waves of depression were converted at the shelf break to elongated waves of depression followed by a packet of elevation waves, as occurs at the ASIAEX-SCS site in the South China Sea. The shallow thermocline conditions at this site may prevent that. However, the waves at the top of Figure 2 could be interpreted as waves of elevation moving shoreward, which would imply that at least some waves can change polarity in the vicinity of Site A when conditions are favorable. Note that with very large internal tides the thermocline can shift downward periodically, so that mode-one nonlinear waves would take the form of elevation waves.

The strong internal tides were characterized with a few weeks of data and compared to ASIAEX-SCS and SW06 internal tides. The total QPE internal tide kinetic energy was greater than was found in SW06, but less than found in ASIAEX. The QPE diurnal internal tide response was strong with respect to the strength of the local diurnal barotropic internal tide. The semidiurnal internal tidal response appears to be weaker than predicted by a numerical model of the M_2 tides in the area.

There are many other internal wave phenomena in the area that were not examined here in detail. Figure 2 clearly shows two of these, southward propagating waves (also seen in the field and tabulated in Fig. 13), and eastward propagating waves. Further study is needed to assess these unexamined waves as well as to more completely understand the four types of waves examined here: The moderate-sized shoaling transbasin waves (moderate compared to Dongsha SCS area), the energetic shallow-water waves of depression, and the two species of internal tide waves.

Acknowledgments. We would like to thank the following: the captain and crew of *RV OR1*, the *OR1* science technicians of National Taiwan University who did an outstanding job under the leadership of Mr. Dai and Mr. Lu, Mark Inall for the Malin Shelf data, and Emily Shroyer for organizing the NDBC station data. Funding for the use of *RV OR1* was provided by the National Science Council of Taiwan. TFD was supported by the Office of Naval Research (ONR) Ocean Acoustics Program under grants N00014-05-1-0482 and N00014-11-1-0194. AEN was supported under ONR grant N00014-08-1-0763, and GG under ONR grant N00014-07-01-0482. HCG and MJC were supported by ONR grants N00014-09-1-0392 and N00014-07-1-0650.

REFERENCES

Apel, J. R.; M. Badiey; C.-S. Chiu; S. Finette; R. Headrick; J. Kemp; J. F. Lynch; A. Newhall; M. H. Orr; B. H. Pasewark; D. Tielbuerger; A. Turgut; K. von der Heydt and S. Wolf. 1997. An overview of the 1995 SWARM shallow-water internal wave acoustic scattering experiment. IEEE J. Oceanic Eng., *22*, 465–500.

Apel, J. R.; L. A. Ostrovsky; Yu. A. Stepanyants, and J. F. Lynch. 2007. Internal solitons in the ocean and their effect on underwater sound. J. Acoust. Soc. Am., *121*, 695–722.

Beardsley, R. C.; T. F. Duda; J. F. Lynch; S. R. Ramp; J. D. Irish; C.-S. Chiu; T. Y. Tang; Y. J. Yang and G. Fang. 2004. Barotropic tide in the northeast South China Sea. IEEE J. Oceanic Eng., *29*, 1075–1086.

Boyd, J. P. 2005. Microbreaking and polycnoidal waves in the Ostrovsky-Hunter equation. Phys. Lett. A., *338*, 36–43.

Duda, T. F.; Y.-T. Lin and D. B. Reeder. 2011. Observationally constrained modeling of sound in curved ocean internal waves: Examination of deep ducting and surface ducting at short range. J. Acoust. Soc. Am., *130*, 1173–1187.

Duda, T. F.; J. F. Lynch; J. D. Irish; R. C. Beardsley; S. R., Ramp; C.-S. Chiu; T.-Y. Tang and Y.-J. Yang. 2004. Internal tide and nonlinear internal wave behavior at the continental slope in the northern South China Sea. IEEE J. Oceanic Eng., *29*, 1105–1130.

Duda, T. F. and L. Rainville. 2008. Diurnal and semidiurnal internal tide energy flux at a continental slope in the South China Sea, J. Geophys. Res., *113*, C03025,

Egbert, G. D. and S. Y. Erofeeva. 2002. Efficient inverse modeling of barotropic ocean tides. J. Atmos. Oceanic Technol., *19*, 183–204.

Gawarkiewicz, G.; S. Jan; P. F. J. Lermusiaux; J. L. McClean; L. Centurioni; K. Taylor; B. Cornuelle; T. F. Duda; J. Wang; Y. J. Yang; T. Sanford; R.-C. Lien; C. Lee; M.-A. Lee; W. Leslie; P. J. Haley Jr.; P. P. Niiler; G. Gopalakrishnan; P. Velez-Belchi; D.-K. Lee and Y. Y. Kim. 2011. Circulation and intrusions northeast of Taiwan: Chasing and predicting uncertainty in the cold dome. Oceanography, *24*, 110–121, http://dx.doi.org/10.5670/oceanog.2011.99.

Green, J. A. M.; J. H. Simpson; S. Legg and M. R. Palmer. 2008. Internal waves, baroclinic fluxes and mixing at the European shelf edge. Cont. Shelf. Res., *28*, 937–950.

Grimshaw, R.; E. Pelinovsky and T. Talipova. 1999. Solitary wave transformation in a medium with sign-variable quadratic nonlinearity and cubic nonlinearity, Physica D, *132*, 40–62.

Helfrich, K. R. and W. K. Melville. 2006. Long nonlinear internal waves, Annu. Rev. Fluid Mech., *38*, 395–425.

Holloway, P. E.; E. Pelinovsky and T. Talipova. 1999. A generalized Korteweg-de Vries model of internal tide transformation in the coastal zone. J. Geophys. Res., *104*, 18,333–18,350.

Jackson, C. 2007. Internal wave detection using the Moderate Resolution Imaging Spectroradiometer (MODIS), J. Geophys. Res., *112*, C11012, doi:10.1029/2007JC004220.

Jan, S.; C.-C. Chen; Y.-L. Tsai; Y. J. Yang; J. Wang; C.-S. Chern; G. Gawarkiewicz; R.-C. Lien; L. Centurioni and J.-Y. Kuo. 2011. Mean structure and variability of the cold dome northeast of Taiwan. Oceanography, *24*(4), 100–109, http://dx.doi.org/10.5670/oceanog.2011.98.

Klymak, J. M.; R. Pinkel; C.-T. Liu; A. K. Liu and L. David. 2006. Prototypical solitons in the South China Sea. Geophys. Res. Lett., *33*, L11607, doi:10.1029/2006GL025932.

Lamb, K. G and K. P. Wilkie. 2004. Conjugate flows for waves with trapped cores. Physics of Fluids, *16*, 4685–4695.

Lavery, A. C.; P. H. Wiebe; T. K. Stanton; G. L. Lawson; M. C. Benfield and N. Copley. 2007. Determining dominant scatterers of sound in mixed zooplankton populations. J. Acoust. Soc. Am. *122*, 3304–3326.

Lee, C .-Y. and R. C. Beardsley. 1974. The generation of long nonlinear internal waves in a weakly stratified shear flow. J. Geophys. Res. *79*, 453–462.

Lermusiaux, P. F. J.; J. Xu; C. F. Chen; S. Jan; L.Y. Chiu and Y.-J. Yang. 2010. Coupled ocean-acoustic prediction of transmission loss in a continental shelfbreak region: Predictive skill, uncertainty quantification and dynamical sensitivities. IEEE J. Oceanic Eng., *35*, 895–916, doi:10.1109/JOE.2010.2068611.

Li, Q.; D. M. Farmer; T. F. Duda and S. Ramp. 2009. Acoustical measurement of nonlinear internal waves using the inverted echo sounder, J. Atmos. Oceanic Technol., *26*, 2228–2242.

Li, Q. and D. M. Farmer. 2011. The generation and evolution of nonlinear internal waves in the deep basin of the South China Sea. J. Phys. Oceanogr., *41*, 1345–1363. http://dx.doi.org/10.1175/2011JPO4587.1

Lien, Ren-Chieh; T. B. Sanford and S. Jan. 2013. Internal tides on East China Sea continental slope. J. Mar. Res, *71*(1-2), 151–186.

Moum, J. N.; D. M. Farmer; W. D. Smyth; L. Armi and S. Vagle. 2003. Structure and generation of turbulence at interfaces strained by internal solitary waves propagating shoreward over the continental shelf. J. Phys. Oceanogr., *33*, 2093–2112.

Nash, J.D.; E.L. Shroyer; S.M. Kelly; M.E. Inall; T.F. Duda; M.D. Levine; N.L. Jones and R.C. Musgrave. 2012. Are any coastal internal tides predictable? Oceanography, *25*, 80–95, http://dx.doi.org/10.5670/oceanog.2012.44.

Newhall, A. E.; T. F. Duda; K. von der Heydt; J. D. Irish; J. N. Kemp; S. A. Lerner; S. P. Liberatore; Y.-T. Lin; J. F. Lynch; A. R. Maffei; A. K. Morozov; A. Shmelev; C. J. Sellers and W. E. Witzell. 2007. Acoustic and oceanographic observations and configuration information for the WHOI moorings from the SW06 experiment, Woods Hole Oceanog. Inst. Tech. Rept., WHOI-2007-04.

Newhall, A. E.; G. G. Gawarkiewicz; J. F. Lynch; T. F. Duda; N. M. McPhee; F. B. Bahr; C. D. Marquette; Y.-T. Lin; S. Jan; J. Wang; C.-F. Chen; L. Y. S. Chiu; Y. J. Yang; R.-C. Wei; C. Emerson; D. Morton; T. Abbot; P. Abbot; B. Calder; L. Mayer and P. F.J. Lermusiaux. 2010. Acoustics and oceanographic observations collected during the QPE Experiment by Research Vessels *OR1, OR2* and *OR3* in the East China Sea in the summer of 2009. Woods Hole Oceanog. Inst. Tech. Rept., WHOI-2010-06.

Niwa, Y. and T. Hibiya. 2004. Three-dimensional numerical simulation of M_2 internal tides in the East China Sea. J. Geophys. Res, *109*, C04027, doi:10.1029/2003JC001923.

Orr, M. H. and P. C. Mignerey. 2003. Nonlinear internal waves in the South China Sea: Observation of the conversion of depression internal waves to elevation internal waves. J. Geophys. Res., *106*, 3064.

Porter, D. L.; D. R. Thompson; W. Alpers and R. Romeiser. 2001. Remotely sensed ocean observations of the Coastal Mixing and Optics site from synthetic aperture radars and advanced very high resolution radiometers. J. Geophys. Res., *106*, 9623–9638, doi:10.1029/2000JC900121.

Ramp, S. R.; T. Y. Tang; T. F. Duda; J. F. Lynch; A. K. Liu; C.-S. Chiu; F. Bahr; H.-R. Kim and Y. J. Yang. 2004. Internal solitons in the northeastern South China Sea part I: Sources and deep water propagation, IEEE J. Oceanic Eng., *29*, 1157–1181.

Ramp, S. R.; Y. J. Yang and F. L. Bahr. 2010. Characterizing the nonlinear internal wave climate in the northeastern South China Sea. Nonlin. Processes Geophys., *17*, 481–498.

Reeder, D. B.; T. F. Duda and B. Ma. 2008. Short-range acoustic propagation variability on a shelf area with strong nonlinear internal waves. In *Oceans '08 Kobe Conference Proceedings*, IEEE, 8 pp.

Scotti, A.; R. C. Beardsley; B. Butman and J. Pineda. 2008. Shoaling of nonlinear internal waves in Massachusetts Bay. J. Geophys. Res., *113*, C08031, doi:10.1029/2008JC004726.

Shroyer, E. L.; J. N. Moum and J. D. Nash, 2010. Energy transformations and dissipation of nonlinear internal waves over New Jersey's continental shelf. Nonlin. Processes Geophys., *17*, 345–360, doi:10.5194/npg-17-345-2010.

Shroyer, E. L.; J. N. Moum and J. D. Nash. 2011. Nonlinear internal waves over New Jersey's continental shelf. J. Geophys. Res, *116*, C03022.

Small, J.; Z. Hallock; G. Pavey and J. Scott. 1999. Observations of large amplitude internal waves at the Malin Shelf edge during SESAME 1995, Cont. Shelf Res., *19*, 1389–1436.

St. Laurent, L. 2008. Turbulent dissipation on the margins of the South China Sea, Geophys. Res. Lett., *35*, L23615, doi:10.1029/2008GL035520.

Turkington, B.; A. Eydeland and S. Wang. 1991. A computational method for solitary internal waves in a continuously stratified fluid. Studies in Applied Math., *85*, 93–127.

Turner, J. S. 1973. *Buoyancy Effects in Fluids*. Cambridge University Press, 368 pp.

Vlasenko V.; P. Brandt and A. Rubino. 2000. Structure of large-amplitude internal solitary waves. J. Phys. Oceanogr., *30*, 2172–2185.

Vlasenko V. and K. Hutter. 2002. Numerical experiments on the breaking of solitary internal waves over a slope-shelf topography. J. Phys. Oceanogr., *32*, 1779–1793.

Vlasenko V.; N. Stashchuk and K. Hutter. 2005. *Baroclinic Tides. Theoretical Modeling and Observational Evidence.* Cambridge University Press, 351 pp.

Yang, Y.-J.; T. Y. Tang; M. H. Chang; A. K. Liu; M.-K. Hsu and S. R. Ramp. 2004. Solitons northeast of Tung-Sha Island during the ASIAEX pilot studies, IEEE J. Oceanic. Eng., *29*, 1182–1199.

Zhao, Z.; V. Klemas; Q. Zheng and X.-H. Yan. 2004. Remote sensing evidence for baroclinic tide origin of internal solitary waves in the northeastern South China Sea, Geophys. Res. Lett., *31*, L06302, doi:10.1029/2003GL019077.

Received: *June 27, 2012*; Revised: *Jan. 31, 2013*.